Systematic KMTNet Planetary Anomaly Search. II. Six New q < 2 x 10-4 Mass-ratio Planets

Kyu-Ha Hwang, Weicheng Zang, Andrew Gould, Andrzej Udalski, Ian A. Bond, Hongjing Yang, Shude Mao, Michael D. Albrow, Sun-Ju Chung, Cheongho Han, et al.

The Astronomical Journal, 163:43 (26pp), 2022 February https://doi.org/10.3847/1538-3881/ac38ad

Systematic KMTNet Planetary Anomaly Search. II. Six New $q < 2 \times 10^{-4}$ Mass-ratio Planets

Kyu-Ha Hwang[1], Weicheng Zang[2], Andrew Gould[3,4], Andrzej Udalski[5], Ian A. Bond[6], Hongjing Yang[2], Shude Mao[2,7] (Lead Authors),
Michael D. Albrow[8], Sun-Ju Chung[1,9], Cheongho Han[10], Youn Kil Jung[1], Yoon-Hyun Ryu[1], In-Gu Shin[1], Yossi Shvartzvald[11], Jennifer C. Yee[12], Sang-Mok Cha[1,13], Dong-Jin Kim[1], Hyoun-Woo Kim[1], Seung-Lee Kim[1,9], Chung-Uk Lee[1,9], Dong-Joo Lee[1], Yongseok Lee[1,13], Byeong-Gon Park[1,9], Richard W. Pogge[4] (KMTNet Collaboration),
Przemek Mróz[14], Radek Poleski[4,5], Jan Skowron[5], Michał K. Szymański[5], Igor Soszyński[5], Paweł Pietrukowicz[5], Szymon Kozłowski[5], Krzysztof Ulaczyk[15], Krzysztof A. Rybicki[5], Patryk Iwanek[5], Marcin Wrona[5], Mariusz Gromadzki[5] (OGLE Collaboration),
Fumio Abe[16], Richard Barry[17], David P. Bennett[17,18], Aparna Bhattacharya[17,18], Hirosame Fujii[16], Akihiko Fukui[19,20], Yuki Hirao[21], Yoshitaka Itow[16], Rintaro Kirikawa[21], Iona Kondo[21], Naoki Koshimoto[22,23], Brandon Munford[24], Yutaka Matsubara[16], Shota Miyazaki[21], Yasushi Muraki[16], Greg Olmschenk[17], Clément Ranc[25], Nicholas J. Rattenbury[24], Yuki K. Satoh[21], Hikaru Shoji[21], Stela Ishitani Silva[17,26], Takahiro Sumi[21], Daisuke Suzuki[27], Paul J. Tristram[28], Atsunori Yonehara[29] (The MOA Collaboration),
and
Xiangyu Zhang[2], Wei Zhu[2], Matthew T. Penny[30], and Pascal Fouqué[31,32] (The Tsinghua & CFHT Microlensing Group)

[1] Korea Astronomy and Space Science Institute, Daejon 34055, Republic of Korea; kyuha@kasi.re.kr
[2] Department of Astronomy and Tsinghua Centre for Astrophysics, Tsinghua University, Beijing 100084, People's Republic of China; weichengzang@qq.com
[3] Max-Planck-Institute for Astronomy, Königstuhl 17, D-69117 Heidelberg, Germany
[4] Department of Astronomy, Ohio State University, 140 W. 18th Avenue, Columbus, OH 43210, USA
[5] Astronomical Observatory, University of Warsaw, Al. Ujazdowskie 4, 00-478 Warszawa, Poland
[6] Institute of Natural and Mathematical Science, Massey University, Auckland 0745, New Zealand
[7] National Astronomical Observatories, Chinese Academy of Sciences, Beijing 100101, People's Republic of China
[8] University of Canterbury, Department of Physics and Astronomy, Private Bag 4800, Christchurch 8020, New Zealand
[9] Korea University of Science and Technology, Korea, (UST), 217 Gajeong-ro, Yuseong-gu, Daejeon, 34113, Republic Of Korea
[10] Department of Physics, Chungbuk National University, Cheongju 28644, Republic Of Korea
[11] Department of Particle Physics and Astrophysics, Weizmann Institute of Science, Rehovot 76100, Israel
[12] Center for Astrophysics | Harvard & Smithsonian, 60 Garden Street, Cambridge, MA 02138, USA
[13] School of Space Research, Kyung Hee University, Yongin, Kyeonggi 17104, Republic Of Korea
[14] Division of Physics, Mathematics, and Astronomy, California Institute of Technology, Pasadena, CA 91125, USA
[15] Department of Physics, University of Warwick, Gibbet Hill Road, Coventry, CV4 7AL, UK
[16] Institute for Space-Earth Environmental Research, Nagoya University, Nagoya 464-8601, Japan
[17] Code 667, NASA Goddard Space Flight Center, Greenbelt, MD 20771, USA
[18] Department of Astronomy, University of Maryland, College Park, MD 20742, USA
[19] Department of Earth and Planetary Science, Graduate School of Science, The University of Tokyo, 7-3-1 Hongo, Bunkyo-ku, Tokyo 113-0033, Japan
[20] Instituto de Astrofísica de Canarias, Vía Láctea s/n, E-38205 La Laguna, Tenerife, Spain
[21] Department of Earth and Space Science, Graduate School of Science, Osaka University, Toyonaka, Osaka 560-0043, Japan
[22] Department of Astronomy, Graduate School of Science, The University of Tokyo, 7-3-1 Hongo, Bunkyo-ku, Tokyo 113-0033, Japan
[23] National Astronomical Observatory of Japan, 2-21-1 Osawa, Mitaka, Tokyo 181-8588, Japan
[24] Department of Physics, University of Auckland, Private Bag 92019, Auckland, New Zealand
[25] Sorbonne Université, CNRS, UMR 7095, Institut d'Astrophysique de Paris, 98 bis bd Arago, F-75014 Paris, France
[26] Department of Physics, The Catholic University of America, Washington, DC 20064, USA
[27] Institute of Space and Astronautical Science, Japan Aerospace Exploration Agency, Kanagawa 252-5210, Japan
[28] University of Canterbury Mt. John Observatory, P.O. Box 56, Lake Tekapo 8770, New Zealand
[29] Department of Physics, Faculty of Science, Kyoto Sangyo University, Kyoto 603-8555, Japan
[30] Department of Physics and Astronomy, Louisiana State University, Baton Rouge, LA 70803 USA
[31] CFHT Corporation, 65-1238 Mamalahoa Hwy, Kamuela, HI 96743, USA
[32] Université de Toulouse, UPS-OMP, IRAP, Toulouse, France
Received 2021 June 11; revised 2021 November 3; accepted 2021 November 3; published 2022 January 5

Abstract

We apply the automated AnomalyFinder algorithm of Paper I to 2018–2019 light curves from the $\simeq$13 deg^2 covered by the six KMTNet prime fields, with cadences $\Gamma \geqslant 2\,\mathrm{hr}^{-1}$. We find a total of 11 planets with mass ratios $q < 2 \times 10^{-4}$, including 6 newly discovered planets, 1 planet that was reported in Paper I, and recovery of 4 previously discovered planets. One of the new planets, OGLE-2018-BLG-0977Lb, is in a planetary caustic event, while the other five (OGLE-2018-BLG-0506Lb, OGLE-2018-BLG-0516Lb, OGLE-2019-BLG-1492Lb, KMT-2019-BLG-0253, and KMT-2019-BLG-0953) are revealed by a "dip" in the light curve as the source crosses the host-planet axis on the opposite side of the planet. These subtle signals were missed in previous by-eye searches. The planet-host separations (scaled to the Einstein radius), s, and planet-host mass ratios, q, are, respectively, $(s,\ q \times 10^5) = (0.88,\ 4.1)$, $(0.96 \pm 0.10,\ 8.3)$, $(0.94 \pm 0.07,\ 13)$, $(0.97 \pm 0.07,\ 18)$, $(0.97 \pm 0.04,\ 4.1)$, and $(0.74,\ 18)$, where the "$\pm$" indicates a discrete degeneracy. The 11 planets are spread out over the range $-5 < \log q < -3.7$. Together with the two planets previously reported with $q \sim 10^{-5}$ from the 2018–2019 nonprime KMT fields, this result suggests that planets toward the bottom of this mass-ratio range may be more common than previously believed.

Unified Astronomy Thesaurus concepts: Gravitational microlensing exoplanet detection (2147)

Supporting material: data behind figures

1. Introduction

By the end of 2005, four microlensing planets had been discovered, of which two were in the low planet-host mass-ratio ($q < 10^{-4}$) regime (Beaulieu et al. 2006; Gould et al. 2006). Twelve years later, there were only seven such discoveries (Udalski et al. 2018) out of a total of more than 60. Moreover, none of these had mass ratios below $q_{\mathrm{thresh,2018.0}} = 4.3 \times 10^{-5}$. The absence of low-$q$ planets in a more restricted but homogeneously selected sample led Suzuki et al. (2016) to argue for a break in the mass-ratio function at about $q_{\mathrm{break}} = 17 \times 10^{-5}$, albeit with a large error bar. That is, they confirmed the earlier finding by Sumi et al. (2010) that above the break the mass-ratio function was a falling power law toward higher mass ratios. Below the break, however, they found that this function was either flat or more likely falling sharply toward lower mass ratios. Based on a larger, though inhomogeneous, sample, Jung et al. (2019b) found the break to be a factor of three lower, $q_{\mathrm{break}} = 5.6 \times 10^{-5}$, but still consistent with Suzuki et al. (2016) within the latter's error bar.

Since the Udalski et al. (2018) study (and prior to this paper), seven additional $q \leqslant 10^{-4}$ planets have been discovered. Five of these seven have mass ratios below the pre-2018 threshold, $q_{\mathrm{thresh,2018.0}} = 4.3 \times 10^{-5}$, and these five were discovered in 2018–2020 data. Although these 14 planets were not homogeneously selected, it is unlikely that this sample is strongly affected by publication bias. That is, $q < 10^{-4}$ planets are relatively rare and are very likely to be published soon after discovery. Only one of the seven recent low-q planets was submitted for publication substantially after discovery, OGLE-2015-BLG-1670 (Ranc et al. 2019).

The very different discovery patterns before and after 2018.0 strongly suggest a systematic difference in the discovery process beginning in 2018 (see Table 1). One possibility is the upgrade in the Korea Microlensing Telescope Network (KMTNet; Kim et al. 2016) online photometry in that year. KMT data played a major or decisive role in all five 2018–2020 discoveries, and many of these planets would have been missed with substantially inferior photometry. For example, KMT-2018-BLG-0029 (Gould et al. 2020) had been the focus of considerable interest during the season because it was targeted for Spitzer observations, yet the few-hour planetary signal at the peak was not noticed until the end-of-year re-reductions, when the new pipeline results were manually reviewed.

Regardless of the exact cause, the changing pattern of discoveries before and after 2018.0 calls for reevaluation of the conclusions regarding the behavior of the mass-ratio function in the $\log q \lesssim -4$ regime. Ultimately, this can only be done on the basis of homogeneous selection of planets, which was a key characteristic of the original Suzuki et al. (2016) study.

Yee et al. (2021) outlined one such approach: make tender-loving care (TLC) reductions of all KMT events meeting a magnification threshold, e.g., $A_{\mathrm{max}} > 20$, and subject these to automated planet searches. This would require improved efficiency of the TLC pipeline to re-reduce so many events.

Zang et al. (2021a) outlined a second approach: intensive follow-up observations of high-magnification events in low-cadence $\Gamma \leqslant 0.4\,\mathrm{hr}^{-1}$ KMT fields. This would be similar to the approach formerly carried out by the Microlensing Follow Up Network (μFUN; Gould et al. 2010), but with much more efficient target selection due to continuous KMT coverage.

Zang et al. (2021b, hereafter Paper I) initiated a third approach: subject the residuals from single-lens single-source (1L1S) fits to the end-of-year pipeline light curves to a search for "bumps" or "dips" based on a modified version of the KMT EventFinder algorithm (Gould 1996; Kim et al. 2018b). At that time, the approach of Paper I could only be applied to 2019 data because the 2016–2017 online reductions were not of sufficiently high quality and the 2018 photometry files lacked some auxiliary data needed for this method. However, the 2018 files have already been updated, and work on the 2016–2017 files is in progress. Note that all three methods are complementary and all could be used simultaneously.

As reported in Paper I, their method recovered the planets in KMT-2019-BLG-0842 (Jung et al. 2020b) and OGLE-2019-BLG-0960 (Yee et al. 2021), i.e., the two previous low-q planets from 2019. And they also reported the discovery of the lowest mass-ratio planetary caustic[33] event to date: OGLE-2019-BLG-1053. Hence, there are good prospects for establishing a large homogeneous sample of $q < 10^{-4}$ planets by applying this technique to several years of KMT data. Here, we begin a program of detailed analysis and publication of all $q < 2 \times 10^{-4}$ planets found from application of the Paper I

[33] There were three planets with comparable mass ratios KMT-2018-BLG-0029 (Gould et al. 2020), OGLE-2019-BLG-0960 (Yee et al. 2021), and KMT-2020-BLG-0414 (Zang et al. 2021a). However, all three were detected via the resonant channel, which, together with the "near-resonant" channel, account for about 3/4 or all published microlensing planets.

Table 1
Summary of Microlensing Planets $q < 10^{-4}$

Years	$q < 4.3 \times 10^{-5}$	$q > 4.3 \times 10^{-5}$	Total
2003–2017	0	8	8
2018–2020	5	1	6
All	5	9	14

method. This will enable a systematic study of the planet mass-ratio function in the regime of the hypothesized break.

We briefly outline the steps leading up to these publications and the steps that are expected to follow. As discussed in Paper I, their automated AnomalyFinder selects potential anomalies based on purely objective criteria applied to KMT light curves. The criteria used here are identical except that we extend the effective timescale range down to $t_{\rm eff} \geqslant 0.05$ days. Three operators (W. Zang, H. Yang, and W. Zhu) then manually and independently select genuine anomalies (or anomalies that could be genuine) based on machine-generated displays. If there are counterparts to the KMT event on the OGLE and/or MOA web pages, then these light curves are checked to determine whether they contradict the apparent KMT anomaly. If so, the anomaly is rejected. If there are no OGLE or MOA data that overlap the anomaly, its reality is checked by visual inspection of the images. Ultimately, we expect to publish all planets (defined as $q < 0.03$) derived from this search, which will eventually be extended to all KMTNet fields and at least the 2016–2019 seasons.

The present paper is based on a search of the KMT database that is restricted to 2018–2019 and to the three pairs of overlapping KMT fields BLG01/BLG41, BLG02/BLG42, and BLG03/BLG43. Each of these fields has a nominal cadence $\Gamma = 2\,{\rm hr}^{-1}$, so the combined cadence is usually $\Gamma = 4\,{\rm hr}^{-1}$. The first restriction is determined by the current state of the photometry files (see above). The second is based on maintaining a stable work flow in what will be a very big project.

In particular, each event that is selected for publication must be subjected to detailed analysis, so their publication in groups does not substantially reduce either the amount of work required or the length of the descriptions.

The long-term goal is to measure the mass-ratio function for the full planetary range $q < 0.03$. To do so, we must measure the sensitivity of the selection process by injecting planets into KMT light curves. Then, two questions will be asked. First, is the anomaly selected by the machine criteria? Second, would this machine-selected candidate ultimately be published? The answer to the first question is unambiguous. The second question is more difficult because it involves several steps that cannot be mimicked for each simulated event, such as re-reduction of the data and systematic searches for alternate models. This analysis is currently in progress (Y. K. Jung et al. 2021, in preparation).

Here, we present six planets, all of which ultimately satisfy $q < 2 \times 10^{-4}$. To construct the present sample, we manually review all anomalous light curves and tentatively classify them by eye into one of five categories: "planet," "planet/binary," "binary/planet," "binary," and "finite source." Among the "planets," we do preliminary 2L1S modeling of all events that could plausibly be $q < 10^{-3}$, using end-of-season pipeline data. Here, nLmS means n lenses and m sources. One of these, OGLE-2018-BLG-0383 (with $q = 2.1 \times 10^{-4}$), was separated out at an early stage as part of an investigation of wide-orbit planets (Wang et al. 2021). For those with $q < 3 \times 10^{-4}$ among the remainder, the KMT data are re-reduced with TLC and then fully analyzed.

All of the other "planets," as well as all of the events in the other four categories, are then cross-matched against events that are published or are known to us to be in preparation. We then cross-match against the very large personal modeling archive of coauthor C. Han. Combined, these cross-matches cover about 75% of all the AnomalyFinder detections. They not only give us good estimates of q for these events but also permit us to check the robustness of our by-eye classifications. Based on this investigation, it is likely that all of the $q < 2 \times 10^{-4}$ planets in the AnomalyFinder sample are contained in the present work. However, we cannot be certain until we complete our systematic investigation of all the anomalous events, which is currently underway.

2. Observations

As outlined in Section 1, all six planets described in this paper were identified in searches of KMT events from its "prime fields," with nominal cadences $\Gamma \geqslant 2\,{\rm hr}^{-1}$, either by the AlertFinder (Kim et al. 2018a) or by the post-season EventFinder (Kim et al. 2018b). KMTNet observes from three identical 1.6 m telescopes, each equipped with a $(2^\circ \times 2^\circ)$ camera at CTIO in Chile (KMTC), SAAO in South Africa (KMTS), and SSO in Australia (KMTA). KMTNet observes primarily in the I band, but in 2018 and 2019 every 10th such observation was complemented by one in the V band.

Five of the six events were independently discovered by the Optical Gravitational Lensing Experiment (OGLE; Udalski et al. 1994; Udalski 2003), using its 1.3 m telescope with 1.4 deg^2 camera at Las Campanas Observatory in Chile. OGLE also observed primarily in the I band, with some V exposures as well.

Two of the six events were independently discovered by the Microlensing Observations in Astrophysics (MOA; Bond et al. 2004) collaboration, using their 1.8 m telescope with 2.2 deg^2 camera at Mt. John in New Zealand, using their $R_{\rm MOA}$ filter, which is roughly the sum of the Cousins R and I bands.

Table 2 gives the catalog names in order of discovery for each event in order to permit information to be easily traced. However, after that, we generally use the first-discovery name. Table 2 also presents the observational cadences Γ, as well as the discovery dates and the sky locations.

In addition, OGLE observed the location of KMT-2019-BLG-0953, and MOA observed the location of the OGLE-2019-BLG-1492 field, although they did not issue alerts for these events. We therefore also incorporate these OGLE and MOA data into the analysis.

Although all six events were alerted in real time, to the best of our knowledge there were follow-up observations for only one: OGLE-2018-BLG-0977. These were from the 3.6 m Canada–France–Hawaii Telescope (CFHT) and were at a cadence of about one per night.

The data were reduced using variants of difference image analysis (DIA; Tomaney & Crotts 1996; Alard & Lupton 1998), as realized by Albrow et al. (2009; KMT), Woźniak (2000; OGLE), Bond et al. (2001; MOA), and Zang et al. (2018; CFHT).

Table 2
Event Names, Cadences, Alerts, and Locations

Name	Γ (hr^{-1})	Alert Date	R.A.$_{J2000}$	Decl.$_{J2000}$	l	b
KMT-2019-BLG-0253	4.0	2 Apr 2019	17:51:31.82	−29:33:55.7	+0.13	−1.43
OGLE-2019-BLG-0410	1.0					
MOA-2019-BLG-127	4.0					
OGLE-2018-BLG-0506	4.0	30 Mar 2018	17:50:31.16	−31:55:26.6	−2.01	−2.45
KMT-2018-BLG-0835	0.3					
OGLE-2018-BLG-0516	0.3	1 Apr 2018	17:58:33.63	−31:15:44.6	−0.57	−3.59
MOA-2018-BLG-107	1.0					
KMT-2018-BLG-0808	2.0					
OGLE-2019-BLG-1492	3.0	6 Oct 2019	18:00:23.15	−28:37:52.1	+1.91	−2.63
KMT-2019-BLG-3004	4.0					
OGLE-2018-BLG-0977	0.8	3 Jun 2018	17:54:01.47	−30:36:17.3	−0.49	−2.42
KMT-2018-BLG-0728	2.0					
KMT-2019-BLG-0953	8.0	27 May 2019	17:57:21.26	−28:40:28.7	+ 1.54	−2.08

3. Light-curve Analyses

3.1. Preamble

There are several features of the light-curve analyses that are common to all six events, which we present in this preamble.

All six events exhibit short perturbations on otherwise standard Paczyński (1986) 1L1S light curves, which are characterized by three parameters (in addition to two flux parameters for each observatory). These are (t_0, u_0, t_E), i.e., the time of lens−source closest approach, the impact parameter (in units of the Einstein radius, θ_E), and the Einstein timescale.

In each case, the anomaly can be localized fairly precisely by eye at t_{anom}, which then yields the offset from the peak, τ_{anom}, and the offset from the host, u_{anom}, both in units of θ_E, as well as the angle α of the source−lens motion relative to the binary axis (Gould & Loeb 1992),

$$\tau_{anom} = \frac{\Delta t_{anom}}{t_E} \equiv \frac{t_{anom} - t_0}{t_E};$$
$$u_{anom}^2 = \tau_{anom}^2 + u_0^2; \quad \tan\alpha = -\frac{u_0}{\tau_{anom}}. \tag{1}$$

Note that this also implies that $u_{anom} = |u_0/\sin\alpha|$.

We define the quantities $s_\pm^\dagger$ by

$$s_\pm^\dagger = \frac{\sqrt{u_{anom}^2 + 4} \pm u_{anom}}{2}. \tag{2}$$

Note that $s_-^\dagger = 1/s_+^\dagger$ and $u_{anom} = s_+^\dagger - s_-^\dagger$. If the source crosses the minor-image (triangular) planetary caustics, then we expect $s \simeq s_-^\dagger$, and if it crosses the major-image (quadrilateral) planetary caustic, then we expect $s \simeq s_+^\dagger$. Here, s is the projected planet-host separation scaled to θ_E. However, only one of the six events analyzed here (OGLE-2018-BLG-0977) has such caustic-crossing features. For the rest, we may expect that the event may be subject to the inner/outer degeneracy identified by Gaudi & Gould (1997). That is, for minor-image perturbations, which are generally characterized by a "dip," roughly the same anomaly can in principle be produced by the source passing "inside" the planetary caustics (closer to the central caustic) or "outside." Then, we may find two solutions, which obey

$$s_-^\dagger = \frac{s_{inner} + s_{outer}}{2} \qquad \text{(minor image)}. \tag{3}$$

For major-image perturbations, which are generally characterized by a "bump," a similar formula applies for $s_+^\dagger$. In the present paper, however, all six planets give rise to minor-image perturbations ("dips").

Gould & Loeb (1992) also show how to make by-eye estimates of q for events in which the source crosses a planetary caustic. Here, we present an extension of their method to estimate q for the case of non-caustic-crossing minor-image perturbations caused by low mass-ratio planets.

We first focus on caustic-crossing events. In this case, there is a demagnification trough between the two flanking caustics, with separation (using notation from Han 2006)

$$\Delta u \simeq 2\eta_{c,1} - \Delta\eta_c = 4\sqrt{\frac{q(s^{-1} - s)}{s}}$$
$$= 4\sqrt{q\frac{u_{anom}}{s}}. \tag{4}$$

Therefore, the duration of the dip in the light curve between the two caustics is $\Delta t_{dip} = (\Delta u/\sin\alpha)t_E$, implying

$$q = \left(\frac{\Delta t_{dip}}{4\, t_E}\right)^2 \frac{s\sin^2\alpha}{u_{anom}}$$
$$= \left(\frac{\Delta t_{dip}}{4\, t_E}\right)^2 \frac{s}{|u_0|}|\sin^3\alpha|. \tag{5}$$

For the case of source trajectories that miss the caustic but still experience a dip (by which the planet is detected), we apply the same formula, but with $s \to s_-^\dagger$, i.e., implicitly assuming that the width of the dip is approximately the same as the separation between the caustics. As shown by Figure 1 of Chung & Lee (2011), this approximation holds best for low mass-ratio lenses $q \lesssim 2 \times 10^{-4}$, which is the main focus of interest here. We do not expect this mass-ratio estimate to be extremely accurate simply because the dip does not itself have precisely defined edges (except in the region of the trough that lies between the

two triangular caustics). Moreover, $\Delta t_{\rm dip}$ enters quadratically into Equation (5). Thus, by contrast with Equations (1) and (2), which should be quite precise, we expect that Equation (5) should be accurate at the factor $\sim$2 level.

Nevertheless, Equation (5) can be quite powerful. Note in particular that for events in which the anomaly occurs at magnifications of at least a few, $A_{\rm anom} \gtrsim 5$, and for which the blending is small compared to the magnified flux, we have $\sin\alpha = u_0/u_{\rm anom} \simeq A_{\rm anom}/A_{\rm max} \simeq 10^{-0.4\Delta I}$, where ΔI is the magnitude offset between the peak and the anomaly. For such cases $s_-^\dagger \to 1 - 0.5/A_{\rm anom} \simeq 1$, and so Equation (5) can be approximated by

$$q \to \frac{10^{-1.2\Delta I}}{u_0}\left(\frac{\Delta t_{\rm dip}}{4\, t_{\rm E}}\right)^2; \quad \text{(limiting form)}. \tag{6}$$

We generally search for seven-parameter "static" (i.e., without lens orbital motion or microlens parallax effects) 2L1S solutions on an (s, q) grid, characterized by $(t_0, u_0, t_{\rm E}, s, q, \alpha, \rho)$, where ρ is the angular source radius scaled to $\theta_{\rm E}$, i.e., $\rho = \theta_*/\theta_{\rm E}$. In the grid search, (s,q) are held fixed at the grid values while $(t_0, u_0, t_{\rm E}, \rho)$ are allowed to vary in a Markov Chain Monte Carlo (MCMC). We use the advanced contour integration code `VBBinaryLensing` (Bozza 2008; Bozza et al. 2018) to calculate the magnification of the 2L1S model, and we identify the best-fit solution via the MCMC method `emcee` (Foreman-Mackey et al. 2013). The three Paczyński parameters $(t_0, u_0, t_{\rm E})$ are seeded at their 1L1S values, and ρ is seeded using the method of Gaudi et al. (2002) at a value near $\rho = \theta_{*,\rm est}/\mu_{\rm typ} t_{\rm E}$, where $\mu_{\rm typ} \equiv 6$ mas yr^{-1} is a typical value of the lens−source relative proper motions, $\mu_{\rm rel}$, and $\theta_{*,\rm est}$ is estimated based on the value of I_s from the 1L1S fit and the KMT-website extinction. For example, $\theta_{*,\rm est} = 0.6\ \mu$as for $I_s - A_I = 18.65$ (Sun-like star) and $\theta_{*,\rm est} = 6\ \mu$as for $I_s - A_I = 14.5$ (clump-like star). The final parameter, α, is seeded at a grid of values around the unit circle, and it is either held fixed or allowed to vary with the chain, depending on circumstances.

After finding one or more local minima on the (s,q)-plane, each local is further refined by allowing all seven parameters to vary in an MCMC.

If it is suspected that microlens parallax effects can be detected or constrained, then four additional parameters are initially added, $\boldsymbol{\pi}_{\rm E} = (\pi_{{\rm E},N}, \pi_{{\rm E},E})$ and $\boldsymbol{\gamma} = ((ds/dt)/s,\ d\alpha/dt)$. Here, $\boldsymbol{\pi}_{\rm E}$ parameterizes the effects of Earth's orbital motion on the light curve (Gould 1992, 2000, 2004),

$$\boldsymbol{\pi}_{\rm E} = \frac{\pi_{\rm rel}}{\theta_{\rm E}}\frac{\boldsymbol{\mu}_{\rm rel}}{\mu_{\rm rel}}; \quad \theta_{\rm E} = \sqrt{\kappa M \pi_{\rm rel}};$$
$$\kappa \equiv \frac{4G}{c^2\,{\rm au}} \simeq 8.14\frac{\rm mas}{M_\odot}, \tag{7}$$

where M is the lens mass and $(\pi_{\rm rel}, \boldsymbol{\mu}_{\rm rel})$ are the lens−source relative (parallax, proper motion), while $(ds/dt, d\alpha/dt)$ are the first derivatives on lens orbital motion. The four parameters must be introduced together, at least initially, because the orbital motion of the lens can mimic the effects on the light curve of orbital motion of Earth (Batista et al. 2011; Skowron et al. 2011). Lens orbital motion can be poorly constrained by the light curve, so that we generally impose a constraint $\beta < 0.8$, where β is the absolute value of the ratio of transverse kinetic to potential energy (An et al. 2002; Dong et al. 2009),

$$\beta = \left|\frac{\rm KE}{\rm PE}\right|_\perp = \frac{\kappa M_\odot {\rm yr}^2}{8\pi^2}\frac{\pi_{\rm E}}{\theta_{\rm E}}\gamma^2\left(\frac{s}{\pi_{\rm E} + \pi_S/\theta_{\rm E}}\right)^3, \tag{8}$$

and where π_S is the source parallax. Strictly speaking, β is only physically constrained to be $\beta < 1$, but combinations of orbits and viewing angles that would generate $\beta > 0.8$ are extremely rare.

When (as usual) the parallax vector $\boldsymbol{\pi}_{\rm E}$ is evaluated in the geocentric frame, it often has elongated, nearly straight contours whose minor axis is aligned with the projected position of the Sun at t_0, i.e., the (negative of the) direction of the Sun's instantaneous apparent direction of acceleration on the plane of the sky. This is because $\pi_{{\rm E},\parallel}$, the component of $\boldsymbol{\pi}_{\rm E}$ that is aligned to this acceleration, induces an asymmetry in the light curve, which leads to strong constraints, whereas $\pi_{{\rm E},\perp}$ induces more subtle, symmetric distortions (Gould et al. 1994; Smith et al. 2003; Gould 2004). Because the right-handed coordinate system $(\pi_{{\rm E},\parallel}, \pi_{{\rm E},\perp})$ is rotated with respect to the (north, east) equatorial coordinates, the tightness of the error ellipse is often not fully reflected when $(\pi_{{\rm E},N}, \pi_{{\rm E},E})$ and their errors are tabulated in papers. In this paper, we therefore also tabulate $(\pi_{{\rm E},\parallel}, \pi_{{\rm E},\perp})$ and their errors in addition to those of $(\pi_{{\rm E},N}, \pi_{{\rm E},E})$. For this purpose, we define ψ as the angle of the minor axis of the parallax ellipse (north through east) rather than the angle of the projected position of the Sun. Of course, there are two such directions, separated by 180°. We choose the one closer to the Sun's apparent acceleration on the sky. In all four events for which the parallax is measurable in the current work, ψ is the same as the Sun's acceleration within one or two degrees. See, e.g., Figure 3 of Park et al. (2004) for an explicit example of the coordinate system.

Even when these so-called "one-dimensional (1D) parallax" measurements fail to constrain the magnitude $|\boldsymbol{\pi}_{\rm E}| = \pi_{\rm E}$, which is what directly enters the mass and distance estimates, they can interact with the Bayesian priors from a Galactic model to constrain the final estimates of these quantities substantially better than $\boldsymbol{\pi}_{\rm E}$ or the Galactic priors do separately.

More generally, $\boldsymbol{\pi}_{\rm E}$ measurements can provide valuable information even when they are consistent with zero. As discussed in the Appendix of Han et al. (2016), no "evidence" of parallax is required to introduce the two $\boldsymbol{\pi}_{\rm E}$ parameters because it is known a priori that $\pi_{\rm E}$ is strictly positive. Hence, measurements that constrain it to be small provide additional information, even if they are formally consistent with zero.

Another important application of 1D parallax measurements is that they can yield a very precise mass estimate when the source and lens are separately resolved many years after the event (Ghosh et al. 2004; Gould 2014). That is, such imaging generally yields a very precise measurement of $\boldsymbol{\mu}_{\rm rel}$, which has the same direction as $\boldsymbol{\pi}_{\rm E}$. Thus, if $\pi_{{\rm E},\parallel}$ is well constrained (and assuming that the $\boldsymbol{\pi}_{\rm E}$ error ellipse is not by chance closely aligned to $\boldsymbol{\mu}_{\rm rel}$), both $\pi_{\rm E}$ and $\theta_{\rm E} = \mu_{\rm rel} t_{\rm E}$ can be precisely determined from such imaging. See Dong et al. (2009) and Bennett et al. (2020) for a case in which the original 1D parallax measurement was turned into lens mass and distance measurements by successively better determinations of $\boldsymbol{\mu}_{\rm rel}$.

3.2. KMT-2019-BLG-0253

In the original automated search for anomalies (Paper I), the deviation in KMT-019-BLG-0253 from the 1L1S model

(Figure 1) was entirely due to KMTC data forming a 0.23-day, roughly linear rising track that lay below the model, centered on HJD′≡ HJD −2,450,000 = 8588.81, i.e., $\Delta t_{\rm anom} = -1.8$ days before the peak. The method aggressively removes bad- or even questionable-seeing and high-background points, which very frequently produce such "features." Nevertheless, because the algorithm examines $\mathcal{O}(10^2)$ nights of data from three observatories on $\mathcal{O}(10^3)$ events, there are numerous such single-observatory deviations even after this aggressive automated culling of the data. Hence, they must be treated with caution. However, after the TLC re-reductions, the previously excluded KMTS points on the same night could be re-included, and these confirmed the dip, whose duration can be estimated as $\Delta t_{\rm dip} = 0.6$ days. Moreover, there are five OGLE points on this night, which generally track the KMTC deviation, including three at the beginning of the night when the dip is pronounced. Finally, dense MOA coverage confirms the subtle "ridge" feature immediately following the dip. Thus, there is no question that the deviation is of astrophysical origin. See Figure 1.

3.2.1. Heuristic Analysis

The 1L1S model yields parameters $t_{\rm E} \simeq 60$ days and $u_0 \simeq 0.06$. The midpoint of the dip is at $\Delta t_{\rm anom} = -2.0$ days and $\Delta t_{\rm dip} = 0.6$ days. Applying the heuristic formalism of Section 3.1, these yield

$$\begin{aligned} \alpha &= 61^\circ; \qquad s \simeq s_-^\dagger \pm \Delta s; \\ s_-^\dagger &= 0.97; \qquad q \sim 7 \times 10^{-5}, \end{aligned} \tag{9}$$

where $\pm\,\Delta s$, which is induced by the offset of the source trajectory from the caustic, cannot be evaluated from the general appearance of the light curve.

3.2.2. Static Analysis

Notwithstanding this seemingly secure reasoning, we conduct a systematic search for 2L1S solutions, as described in Section 3.1. As expected, we find two solutions, which we then seed into two MCMCs in which all parameters are allowed to vary. The resulting parameters are shown in Table 3. As can be seen from Figure 1, the two model light curves are virtually indistinguishable. A classic case of this inner/outer degeneracy for the minor-image perturbation is presented by Calchi Novati et al. (2019). However, in contrast to that case, the "outer" solution does not have a planetary caustic (outside of which the source would pass). Rather, the planetary and central caustics have merged into a single resonant caustic (e.g., Gaudi 2012), and the "outer" solution passes outside the "planetary wing" of this resonant caustic (see Figure 2). Within the context of the heuristic treatment of Section 3.2.1, we find from Table 3 that the two solutions can be represented as $(s_-^\dagger \pm \Delta s) = (0.969 \pm 0.040)$, while $\alpha = 59^\circ$. Both are in good agreement with Equation (9). By contrast, the static model mass ratio, $q = 4.1 \times 10^{-5}$, is almost a factor of two smaller than the heuristic estimate.

We note that the (s, α) geometry, caustic topology, and inner/outer degeneracy of OGLE-2018-BLG-0677 (Herrera-Martin et al. 2020) are the same as for KMT-2019-BLG-0253, except that the anomaly comes just after the peak, while it comes just before peak for KMT-2019-BLG-0253. In that case, $(s_-^\dagger \pm \Delta s) = (0.95 \pm 0.03)$, which is also very similar to the present case.

The case of OGLE-2016-BLG-1195 (Bond et al. 2017; Shvartzvald et al. 2017) is also closely related. It likewise has an inner/outer degeneracy, with the outer solution having a resonant caustic. However, in that case the source intersected the binary axis on the planet's side of the host rather than the opposite side. Hence, $s_+^\dagger > 1$, i.e., $(s_+^\dagger \pm \Delta s) = (1.03 \pm 0.05)$, compared to $s_-^\dagger < 1$ for KMT-2019-BLG-0253 and OGLE-2018-BLG-0677. OGLE-2019-BLG-0960 (Yee et al. 2021) is yet another example of a major-image anomaly induced by a similar caustic topology, with $(s_+^\dagger \pm \Delta s) = (1.012 \pm 0.015)$.

3.2.3. Parallax Analysis

In the static solution, the event timescale is a substantial fraction of a year, which implies that it may be possible to measure the annual-parallax effect due to Earth's orbital motion. As mentioned in Section 3.1, we must at least initially also introduce the linearized orbital motion parameters $\boldsymbol{\gamma}$. However, we find that the orbital motion parameters are neither significantly constrained nor significantly correlated with the parallax parameters. Therefore, we suppress these 2 degrees of freedom (dof).

We initially find a seemingly strongly constrained and large value of $\pi_{\rm E}$. However, after conducting several tests, we conclude that this signal is the result of systematics in the KMT data. First, by examining the cumulative distribution, $\Delta\chi^2(t) = \chi^2(t;\,\text{static}) - \chi^2(t;\,\text{parallax})$, we find that the great majority of the "signal" comes from late in the light curve, $t > t_0 + 2\,t_{\rm E}$. It is nearly impossible to arrange a physical situation for which this would be the case. Moreover, this "signal" appears only in the KMT data and not in the OGLE data. With fewer data points, we would expect the signal to be weaker in OGLE but still present. Finally, two KMT observatories (KMTS and KMTA) show strongly increasing $\Delta\chi^2(t)$ during these late times, while the third is strongly decreasing. We also considered that this "signal" might be due to "xallarap," i.e., orbital motion of the source about an unseen companion, rather than orbital motion of Earth. Indeed, there was a stronger xallarap signal than parallax signal. However, the same inconsistencies between data sets persisted. And this continued when we fit for parallax and xallarap simultaneously. We attempted to eliminate only these late-time KMT data, but similar signatures of systematics remained, albeit at a lower level. We are not certain what is the cause of these systematics, which affect all three KMT telescopes, but in different directions. We note that there are several bright variable stars in the field, though none closer than 20″. These, in principle, could affect KMT photometry at a very low level, without affecting OGLE photometry, which is overall better. Then, the very large number of these points could amplify the small "signal" in each to create strong trends.

We therefore measure $\boldsymbol{\pi}_{\rm E}$ by fitting only to OGLE data, but with the planet parameters (s, q, α, ρ) held fixed at those of the static solution. The results are shown in Table 3. There are two points to note. First, the axis ratio of the error ellipse, $\sigma(\pi_{\rm E,\perp})/(\sigma(\pi_{\rm E,\parallel})$, is large, ranging from 15 to 20, depending on the solution. That is, this is a 1D parallax measurement. Second, $|\pi_{\rm E,\parallel}|/\sigma(\pi_{\rm E,\parallel}) \simeq 3$, indicating that the parallax is robustly detected. In fact, we find a very similar value for this parameter from the full data set but with much smaller errors $\pi_{\rm E,\parallel} \simeq -0.100 \pm 0.009$. As $\pi_{\rm E,\parallel}$ is much less prone to systematics than $\pi_{\rm E,\perp}$, we take this as qualitative confirmation of the correctness of the $\pi_{\rm E,\parallel}$ measurement.

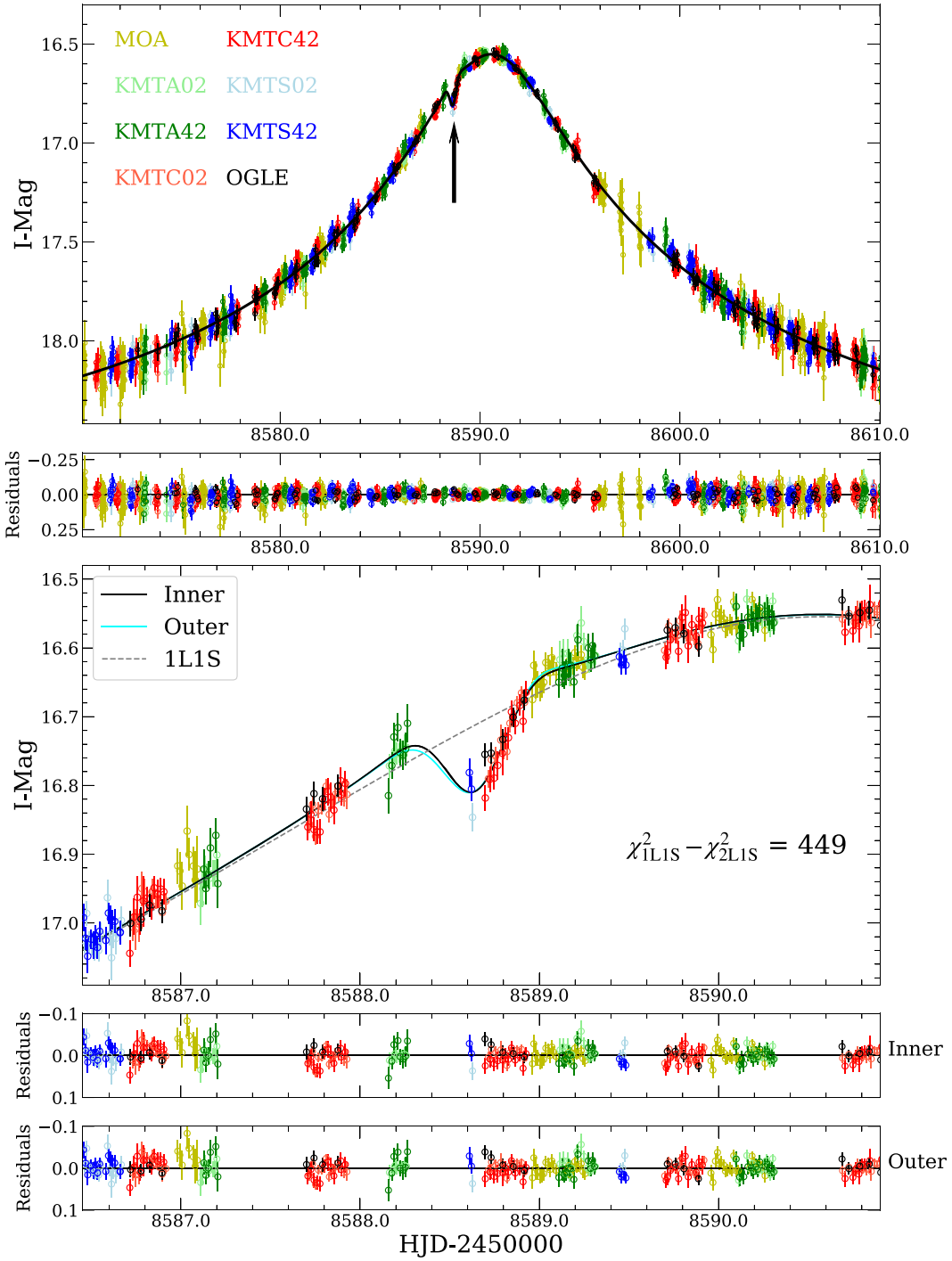

Figure 1. Light curve and models of KMT-2019-BLG-0253. The main evidence for the "inner" and "outer" planetary model (which are virtually identical) is the "dip" in KMTC data from Chile, near 8588.6. This dip is supported by contemporaneous OGLE data, also from Chile, and also by two points from KMTS in South Africa. The dip is the signature of a minor-image perturbation, passing either "inside" or "outside" the two triangular caustics associated with the minor image. See Figure 2. (The data used to create this figure are available.)

We note that ρ is not constrained to be different from zero at the 3σ level. Rather, there is only an upper limit on ρ, which arises because if ρ were sufficiently large, the "dip" would be more rounded than is actually the case. In fact, this will prove to be the case for all six events presented here. Nevertheless, this upper limit on ρ (so lower limit on $\theta_E = \theta_*/\rho$) can help constrain the physical interpretation of the event, as we discuss in Section 5.

For completeness, we report the static solutions for the OGLE-only data set: $(\chi^2, t_0, u_0, t_E, I_S) = (1653.7,\ 8590.5587 \pm 0.0134,\ 0.0558 \pm 0.0018,\ 56.35 \pm 1.53,\ 19.771 \pm 0.036)$ and $(1652.7,\ 8590.5686 \pm 0.0144,\ 0.0576 \pm 0.0018,\ 54.91 \pm 1.46,\ 19.735 \pm 0.035)$ for the inner and outer solutions, respectively. Because there are of order 9 times fewer OGLE points compared to OGLE +KMT, we expect that the errors will be of order $\sqrt{9} = 3$ times

Table 3
2L1S Parameters for KMT-2019-BLG-0253

Parameters	Static		Parallax			
	Inner	Outer	Inner $u_0 > 0$	Inner $u_0 < 0$	Outer $u_0 > 0$	Outer $u_0 < 0$
χ^2	14,661.2	14,660.9	1640.0	1640.2	1642.0	1641.9
dof	14,661	14,661	1640	1640	1640	1640
t_0	8590.5774	8590.5814	8590.5618	8590.5552	8590.5645	8590.5599
	0.0053	0.0055	0.0183	0.0162	0.0172	0.0154
u_0	0.0555	0.0559	0.0538	−0.0532	0.0565	−0.0566
	0.0006	0.0006	0.0034	0.0035	0.0026	0.0027
t_E (days)	57.01	56.66	58.77	59.60	56.08	55.76
	0.55	0.52	4.13	4.13	2.74	2.80
s	0.9289	1.0092	…	…	…	…
	0.0074	0.0088	…	…	…	…
q (10^{-5})	4.07	4.10	…	…	…	…
	0.75	0.72	…	…	…	…
α (rad)	1.0230	1.0223	…	…	…	…
	0.0043	0.0041	…	…	…	…
ρ	<0.0045	<0.0045	…	…	…	…
$\pi_{E,N}$	…	…	−0.550	0.509	−0.362	0.198
	…	…	0.609	0.490	0.482	0.445
$\pi_{E,E}$	…	…	0.028	0.114	0.053	0.102
	…	…	0.074	0.038	0.062	0.036
$\pi_{E,\parallel}$	…	…	−0.089	−0.089	−0.094	−0.092
	…	…	0.030	0.030	0.029	0.029
$\pi_{E,\perp}$	…	…	−0.544	0.514	−0.354	0.203
	…	…	0.613	0.491	0.485	0.445
ψ (deg)	…	…	276.4	272.8	276.5	272.8
$I_{S,\ KMTC02}$	19.780	19.771	19.665	19.680	19.611	19.607
	0.012	0.012	0.071	0.074	0.051	0.054

Note. For parallax solutions, (s, q, ρ, α) are held fixed at their static values, and only the OGLE data are included in the fit. The upper limits on ρ are at 3σ.

larger than those of the static solutions from the full data set, and this expectation is confirmed by comparison to Table 3. Within these errors, the static and parallax solutions are consistent for these parameters.

Comparing the OGLE-only static and parallax fits, we see that the errors in the latter are of order two times larger for (u_0, t_E, I_S). This is partially explained by correlations between each of these three parameters and $\pi_{E,\perp}$. That is, to leading order, $\pi_{E,\parallel}$ and $\pi_{E,\perp}$ give rise to light-curve distortions that are, respectively, antisymmetric and symmetric in $(t - t_0)$ (Smith et al. 2003; Gould 2004). Because the Paczyński (1986) formula is even in $(t - t_0)$ for (u_0, t_E, I_S), these three parameters are correlated with $\pi_{E,\perp}$, which has a large uncertainty. We note that this same effect is present in the three other events with parallax solutions that are analyzed below, although it is strongest in the case of KMT-2019-BLG-0253.

3.3. OGLE-2018-BLG-0506

Figure 3 shows a clear $\Delta I \sim 0.06$ mag dip in the KMTC data at $\Delta t_{anom} \sim 0.54$ days after the peak, with a duration $\Delta t_{dip} = 0.4$ days. The depression defined by these 26 data points, which are taken in good seeing (1.″2–1.″6) and low background, is confirmed by the two contemporaneous OGLE points. Hence, the anomaly is secure.

3.3.1. Heuristic Analysis

The 1L1S model yields parameters $t_E \simeq 24$ days and $u_0 \simeq 0.09$. As noted above, $\Delta t_{anom} = +0.54$ days and $\Delta t_{dip} = 0.4$ days. Applying the heuristic formalism of Section 3.1, these yield

$$\begin{aligned} \alpha &= 104°;\ s \simeq s_-^\dagger \pm \Delta s; \\ s_-^\dagger &= 0.95;\ q \sim 17 \times 10^{-5}. \end{aligned} \tag{10}$$

Again, $\pm \Delta s$, which is induced by the offset of the source trajectory from the caustic, cannot be evaluated from the general appearance of the light curve.

3.3.2. Static Analysis

The grid search described in Section 3.1 returns two local minima, which we then further refine by allowing all parameters to vary in the MCMC. The resulting solutions are given in Table 4 and illustrated in Figure 3. The two solutions can be represented as $(s_-^\dagger \pm \Delta s) = (0.961 \pm 0.099)$, while $\alpha = 106°$, both in good agreement with Equation (10). The mass ratios of the two solutions are $q_{inner} = (7.8 \pm 2.3) \times 10^{-5}$ and $q_{outer} = (7.6 \pm 2.3) \times 10^{-5}$, respectively. Note that these measurements are in only qualitative agreement with the estimate in Equation (10).

Figure 2 shows that the caustic topologies are identical to the case of KMT-2019-BLG-0253. That is, for the inner solution the source traverses the trough that extends along the minor-image axis between the central and planetary caustics, while in the outer solution these two triangular caustics have merged into a resonant caustic.

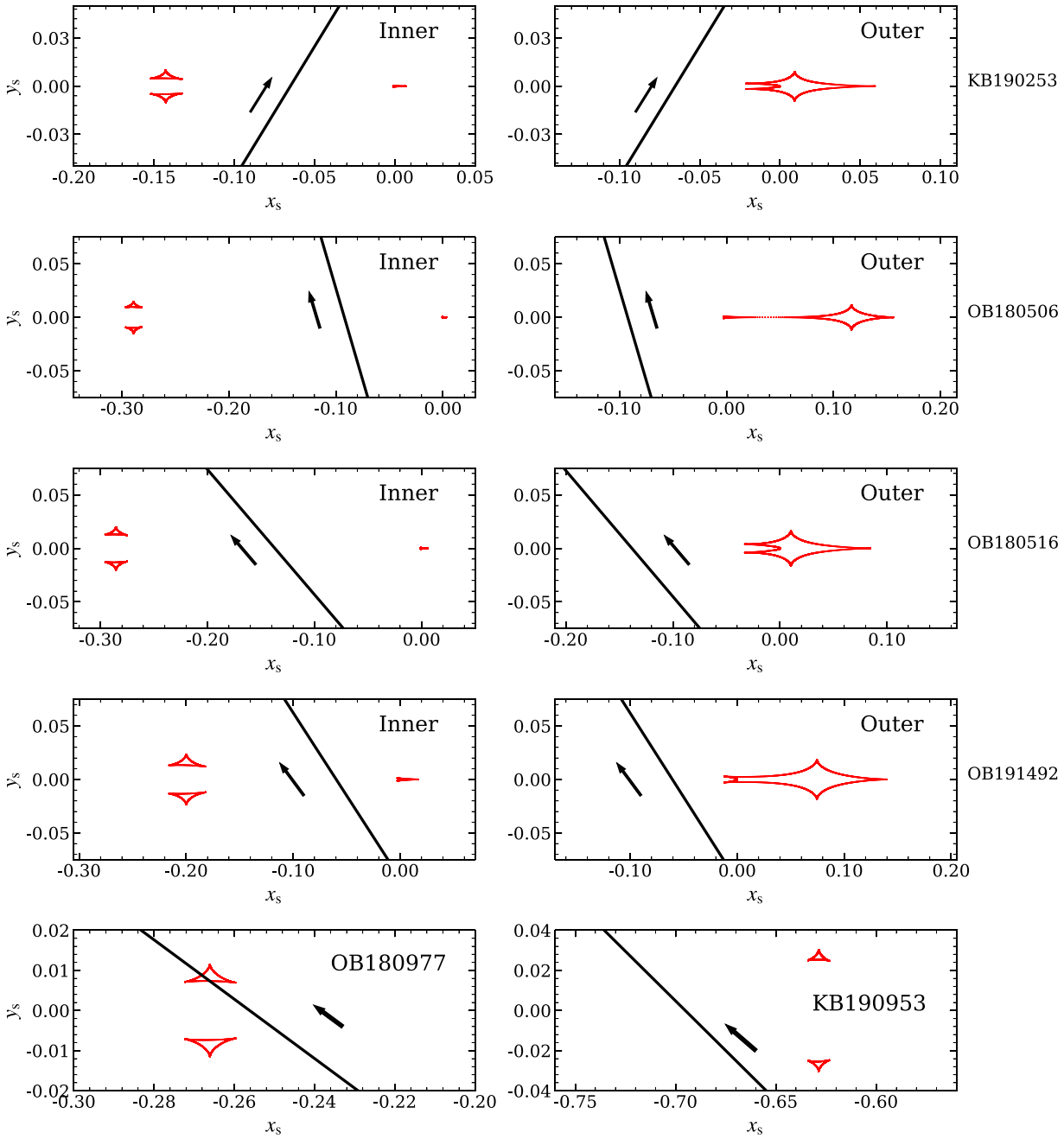

Figure 2. Caustic topologies for all six events. For the first four, the degenerate pairs have identical topologies. In each case, for the "inner" topology, the source passes between the central caustic and the two triangular caustics associated with the minor image (opposite side of host from the planet). The "dip" is due to a magnification trough that runs along the planet-host axis, between these caustics. For the "outer" topology, these caustics have merged with the central caustic to form a resonant caustic. The "dip" is then due to the magnification trough that extends out from between these two wings of the resulting resonant caustic. For OGLE-2018-BLG-0977, the source intersects the triangular caustics, so there is no degeneracy. For KMT-2019-BLG-0953, there is only an "outer" solution. See Section 3.7.2.

3.3.3. Parallax Analysis

The timescale of this event is relatively short, and the source is faint. Therefore, we do not expect to be able to measure the microlens parallax $\boldsymbol{\pi}_{\rm E}$. Nevertheless, as a matter of due diligence, we explore this possibility. We first find, after including both $\boldsymbol{\pi}_{\rm E}$ and the lens orbital parameters $\boldsymbol{\gamma}$, that the latter are not meaningfully constrained (relative to the physical condition $\beta < 0.8$). Hence, we suppress these 2 dof. As in the case of KMT-2019-BLG-0253, correlated errors in the KMT baseline data induced spurious parallax signals, but in contrast to that case, there was no evidence of spurious signals in the body of this event. Hence, most KMT baseline data were removed, i.e., roughly 70% of the full-year KMT data set. For consistency, the same cuts were applied for the static fits. The results are given in Table 4. These show that both $\pi_{\rm E,\parallel}$ and $\pi_{\rm E,\perp}$ are consistent with zero at the 1σ level, which is reflected by the fact that χ^2 is essentially unchanged by the addition of 2 dof. Nevertheless, the fact that $\pi_{\rm E,\parallel}$ is constrained to be near zero within relatively small errors can be a significant constraint in the Bayesian analysis of Section 5. Moreover, none of the other parameters are significantly affected by the inclusion of $\boldsymbol{\pi}_{\rm E}$ in the fit. We therefore adopt the parallax solutions for our final result.

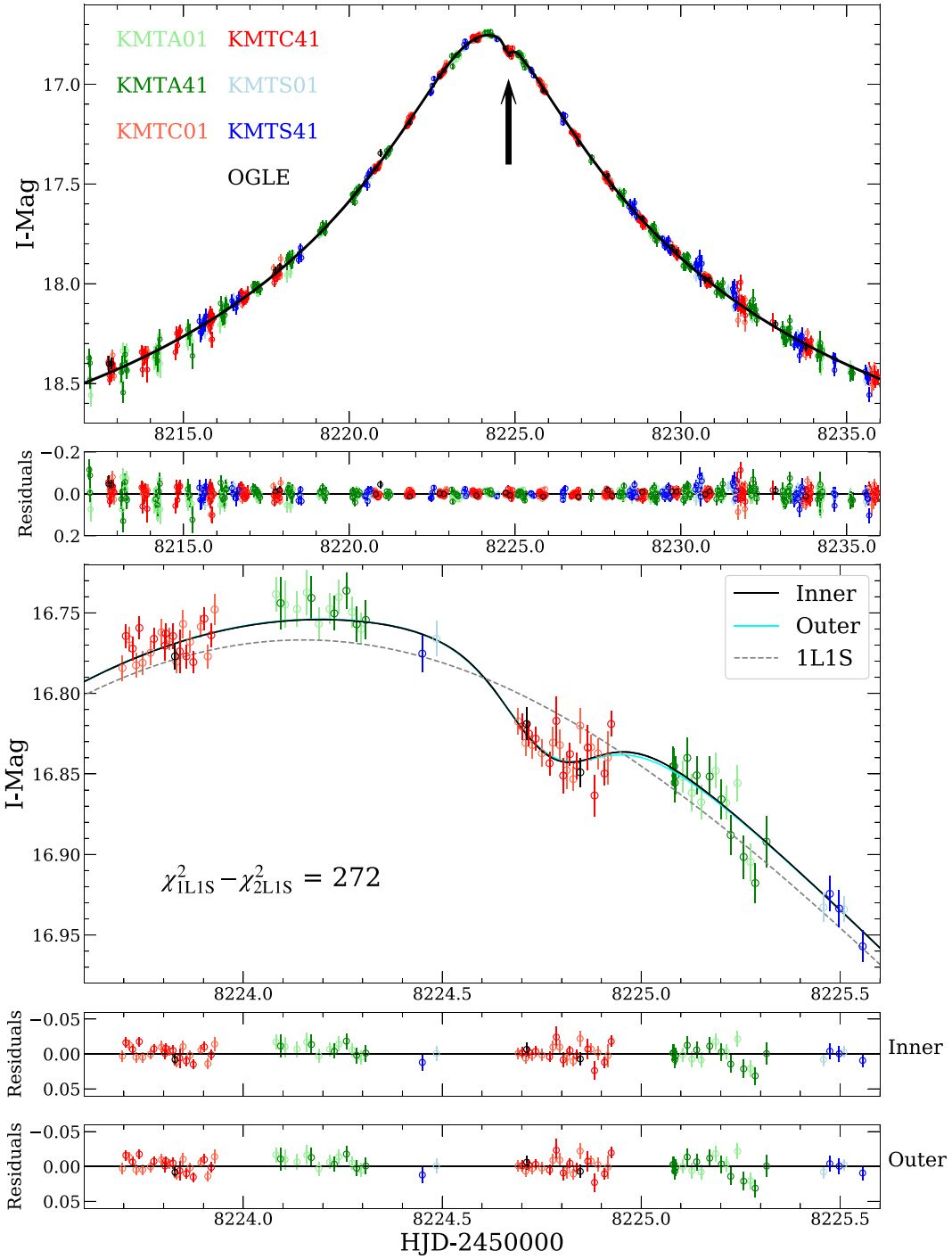

Figure 3. Light curve and models of OGLE-2018-BLG-0506. The main evidence for an anomaly comes from the dip at about 8224.7 as seen in 26 KMTC points. This is confirmed by two OGLE points. The caustic topology is the same as for KMT-2019-BLG-0253. See Figure 2.

(The data used to create this figure are available.)

3.4. OGLE-2018-BLG-0516

Again, there is clear dip in the light curve, which has $\Delta t_{\rm anom} = 2.2$ days and duration $\Delta t_{\rm dip} = 0.5$ days. It is most clearly defined by KMTC data, but these are supported by contemporaneous OGLE data. Moreover, the beginning of the dip is traced by KMTS data, while the end of the dip is supported by both MOA and KMTA data. Hence, the anomaly is secure.

3.4.1. Heuristic Analysis

The 1L1S model yields parameters $t_{\rm E} \simeq 25$ days and $u_0 \simeq 0.10$. As noted above, $\Delta t_{\rm anom} = 2.2$ days and $\Delta t_{\rm dip} = 0.5$ days. Applying the heuristic formalism of Section 3.1, these yield

$$\begin{aligned} \alpha &= 131^\circ; \quad s \simeq s_-^\dagger \pm \Delta s; \\ s_-^\dagger &= 0.93; \quad q \sim 10 \times 10^{-5}. \end{aligned} \tag{11}$$

Table 4
2L1S Parameters for OGLE-2018-BLG-0506

Parameters	Static		Parallax			
	Inner	Outer	Inner $u_0 > 0$	Inner $u_0 < 0$	Outer $u_0 > 0$	Outer $u_0 < 0$
χ^2	2998.2	2997.8	2996.0	2995.9	2995.7	2995.5
dof	2998	2998	2996	2996	2996	2996
t_0	8224.1580	8224.1584	8224.1577	8224.1577	8224.1581	8224.1580
	0.0026	0.0028	0.0046	0.0042	0.0046	0.0041
u_0	0.0884	0.0884	0.0878	−0.0878	0.0879	−0.0878
	0.0012	0.0012	0.0014	0.0013	0.0013	0.0014
t_E (days)	23.86	23.87	23.84	23.81	23.85	23.84
	0.28	0.28	0.35	0.33	0.35	0.37
s	0.8612	1.0594	0.8564	0.8548	1.0673	1.0653
	0.0176	0.0214	0.0153	0.0148	0.0188	0.0189
q (10^{-5})	7.78	7.63	8.22	8.48	8.46	8.16
	2.26	2.34	2.33	2.32	2.35	2.33
α (rad)	1.8536	1.8532	1.8546	−1.8541	1.8544	−1.8554
	0.0065	0.0067	0.0077	0.0084	0.0078	0.0080
ρ	<0.012	<0.014	<0.012	<0.012	<0.014	<0.014
$\pi_{E,N}$	⋯	⋯	0.621	−0.794	0.495	−0.752
	⋯	⋯	1.636	1.637	1.645	1.683
$\pi_{E,E}$	⋯	⋯	0.018	−0.094	0.006	−0.090
	⋯	⋯	0.145	0.125	0.147	0.128
$\pi_{E,\parallel}$	⋯	⋯	0.035	0.036	0.037	0.035
	⋯	⋯	0.034	0.034	0.035	0.034
$\pi_{E,\perp}$	⋯	⋯	0.620	−0.799	0.494	−0.757
	⋯	⋯	1.642	1.641	1.652	1.687
ψ (deg)	⋯	⋯	274.9	274.2	275.0	274.2
$I_{S,\ KMTC01}$	19.163	19.163	19.170	19.169	19.169	19.170
	0.015	0.015	0.017	0.017	0.016	0.017

Note. The upper limits on ρ are at 3σ.

Again, $\pm\,\Delta s$ cannot be determined at this level of analysis.

3.4.2. Static Analysis

The grid search described in Section 3.1 returns two local minima, which we then further refine by allowing all parameters to vary in the MCMC. The resulting solutions are given in Table 5 and illustrated in Figure 4. The two solutions can be represented as $(s_-^\dagger \pm \Delta s) = (0.936 \pm 0.069)$, while $\alpha = 130°$, in good agreement with Equation (11). The mass ratios of the two solutions are $q_{\rm inner} = (12.9 \pm 1.4) \times 10^{-5}$ and $q_{\rm outer} = (13.2 \pm 1.4) \times 10^{-5}$, respectively, which are also in good agreement with Equation (11).

Figure 2 shows that the caustic topologies are again identical to the cases of KMT-2019-BLG-0253 and OGLE-2018-BLG-0506.

3.4.3. Parallax Analysis

The overall situation here is similar to that of OGLE-2018-BLG-0506 (Section 3.3.3). However, in contrast to that case, there were no spurious signals from the KMT baseline data, so the full data set was included in the fit. Again, we test for and then suppress the orbital motion parameters $\boldsymbol{\gamma}$. In this case, we find that $\pi_{E,\parallel}$ is consistent with zero at the $\simeq 1.5\sigma$ level, so the χ^2 improvement is $\simeq 2$ for 2 dof. Again, we find little difference for the other parameters between the static and parallax analyses. And again, we adopt the parallax solution for our final result, noting that the $\pi_{E,\parallel}$ constraint can play some role in the Bayesian analysis of Section 5.

3.5. OGLE-2019-BLG-1492

Again, there is clear dip in the light curve, which has $\Delta t_{\rm anom} = +1.6$ days and duration $\Delta t_{\rm dip} = 0.8$ days. It is most clearly defined by KMTC data, but these are supported by contemporaneous OGLE data. Moreover, there are "ridges" around the dip, which are supported by all observatories.

3.5.1. Heuristic Analysis

The 1L1S model yields parameters $t_E \simeq 50$ days and $u_0 \simeq 0.05$. As noted above, $\Delta t_{\rm anom} = 1.6$ days and $\Delta t_{\rm dip} = 0.8$ days. Applying the heuristic formalism of Section 3.1, these yield

$$\begin{aligned} \alpha &= 123°; \quad s \simeq s_-^\dagger \pm \Delta s; \\ s_-^\dagger &= 0.97; \quad q \sim 18 \times 10^{-5}. \end{aligned} \tag{12}$$

Again, $\pm\,\Delta s$ cannot be determined at this level of analysis.

3.5.2. Static Analysis

The grid search described in Section 3.1 returns two local minima, which we then further refine by allowing all parameters to vary in the MCMC. The resulting solutions are given in Table 6 and illustrated in Figure 5. The two solutions can be represented as $(s_-^\dagger \pm \Delta s) = (0.971 \pm 0.073)$, while $\alpha = 122°$, in good agreement with Equation (12). The mass ratios of the two solutions are $q_{\rm inner} = (19.1 \pm 5.8) \times 10^{-5}$ and $q_{\rm outer} = (17.6 \pm 5.4) \times 10^{-5}$, respectively, which are in good agreement with Equation (12).

Table 5
2L1S Parameters for OGLE-2018-BLG-0516

Parameters	Static		Parallax			
	Inner	Outer	Inner $u_0 > 0$	Inner $u_0 < 0$	Outer $u_0 > 0$	Outer $u_0 < 0$
χ^2	5074.4	5067.7	5072.4	5072.7	5065.7	5065.8
dof	5068	5068	5066	5066	5066	5065
t_0	8227.6483	8227.6514	8227.6515	8227.6513	8227.6541	8227.6542
	0.0055	0.0054	0.0057	0.0058	0.0061	0.0057
u_0	0.1042	0.1050	0.1034	−0.1034	0.1044	−0.1042
	0.0013	0.0014	0.0015	0.0016	0.0015	0.0015
t_E (days)	24.96	24.85	25.47	25.12	25.06	24.97
	0.25	0.25	0.39	0.39	0.37	0.36
s	0.8674	1.0055	0.8679	0.8676	1.0059	1.0063
	0.0041	0.0048	0.0042	0.0043	0.0047	0.0048
q (10^{-5})	12.90	13.18	12.80	12.92	12.99	13.13
	1.35	1.40	1.34	1.44	1.46	1.42
α (rad)	2.2775	2.2754	2.2733	−2.2764	2.2718	−2.2749
	0.0039	0.0037	0.0087	0.0093	0.0077	0.0081
ρ	<0.011	<0.011	<0.011	<0.011	<0.011	<0.011
$\pi_{E,N}$	⋯	⋯	−0.461	0.078	−0.510	0.070
	⋯	⋯	1.049	1.094	0.938	0.999
$\pi_{E,E}$	⋯	⋯	−0.108	−0.054	−0.111	−0.053
	⋯	⋯	0.113	0.092	0.105	0.084
$\pi_{E,\parallel}$	⋯	⋯	0.062	0.060	0.058	0.058
	⋯	⋯	0.041	0.039	0.041	0.041
$\pi_{E,\perp}$	⋯	⋯	−0.469	0.074	−0.519	0.066
	⋯	⋯	1.054	1.097	0.943	1.002
ψ (deg)	⋯	⋯	275.7	274.4	275.9	274.2
$I_{S,\ KMTC01}$	19.420	19.411	19.429	19.429	19.419	19.420
	0.014	0.015	0.017	0.018	0.016	0.017

Note. The upper limits on ρ are at 3σ.

Figure 2 shows that the caustic topologies are again identical to the cases of KMT-2019-BLG-0253, OGLE-2018-BLG-0506, and OGLE-2018-BLG-0516.

3.5.3. Parallax Analysis

The situation here is similar to that of OGLE-2018-BLG-0506 (Section 3.4.3). Spurious parallax signals from the KMT baseline force us to remove most of these data points, corresponding to about half of the full-year KMT data set. Again, we test for and then suppress the orbital motion parameters $\boldsymbol{\gamma}$. Again, we find that $\boldsymbol{\pi}_E$ is only weakly constrained (and only in the $\pi_{E,\parallel}$ direction). Again, we find little difference for the other parameters between the static and parallax analyses. And again, we adopt the parallax solution for our final result.

3.6. OGLE-2018-BLG-0977

The KMTS data show a strong and sudden dip ending in a flat minimum, which is characteristic of the source passing into the trough between the two triangular minor-image caustics, with the entrance close to one of these caustics. One therefore expects the source to pass over the other caustic, an expectation that is confirmed by the rapid drop of the KMTA data during the first three points of the night, which span 69 minutes. Thus, KMTS and KMTA give independent and completely consistent evidence for a minor-image caustic crossing.

The center of the dip occurs $\Delta t_{\rm anom} = +4.0$ days after peak. Because the source crosses the two triangular caustics, the $\Delta t_{\rm dip} = 0.5$-day depression is a much more clearly defined structure than in the four previous cases.

3.6.1. Heuristic Analysis

The 1L1S model yields parameters $t_E \simeq 20$ days and $u_0 \simeq 0.15$. As noted above, $\Delta t_{\rm anom} = +4.0$ days and $\Delta t_{\rm dip} = 0.5$ days. Applying the heuristic formalism of Section 3.1, these yield

$$\alpha = 143°;\ s = s_-^\dagger = 0.88;\ q \simeq 5 \times 10^{-5}. \quad (13)$$

That is, because the source crosses the planetary caustic, there is only one solution. In such cases, we expect the mass-ratio estimate to be quite accurate.

3.6.2. Static Analysis

The grid search described in Section 3.1 returns only one local minimum, which we then further refine by allowing all parameters to vary in the MCMC. We find that, due to the extreme faintness of the source $I_S \sim 21$ and shortness of the event ($t_E = 20$ days), correlations in the KMT baseline data impact even the static fit. We therefore eliminate these data, keeping only $8260 < \mathrm{HJD}' < 8296$. The resulting solution is given in Table 7 and illustrated in Figure 6. In particular, $(s,\ q,\ \alpha) = (0.879,\ 4.15 \times 10^{-5},\ 144°)$, in good agreement with Equation (13).

Figure 2 shows that, as expected, and in contrast to the previous four events, the source crosses the caustic.

3.6.3. Parallax Analysis

When we incorporate $\boldsymbol{\pi}_E$ and $\boldsymbol{\gamma}$ into the fits, we find that neither is meaningfully constrained. Therefore, we adopt the parameters of the static model.

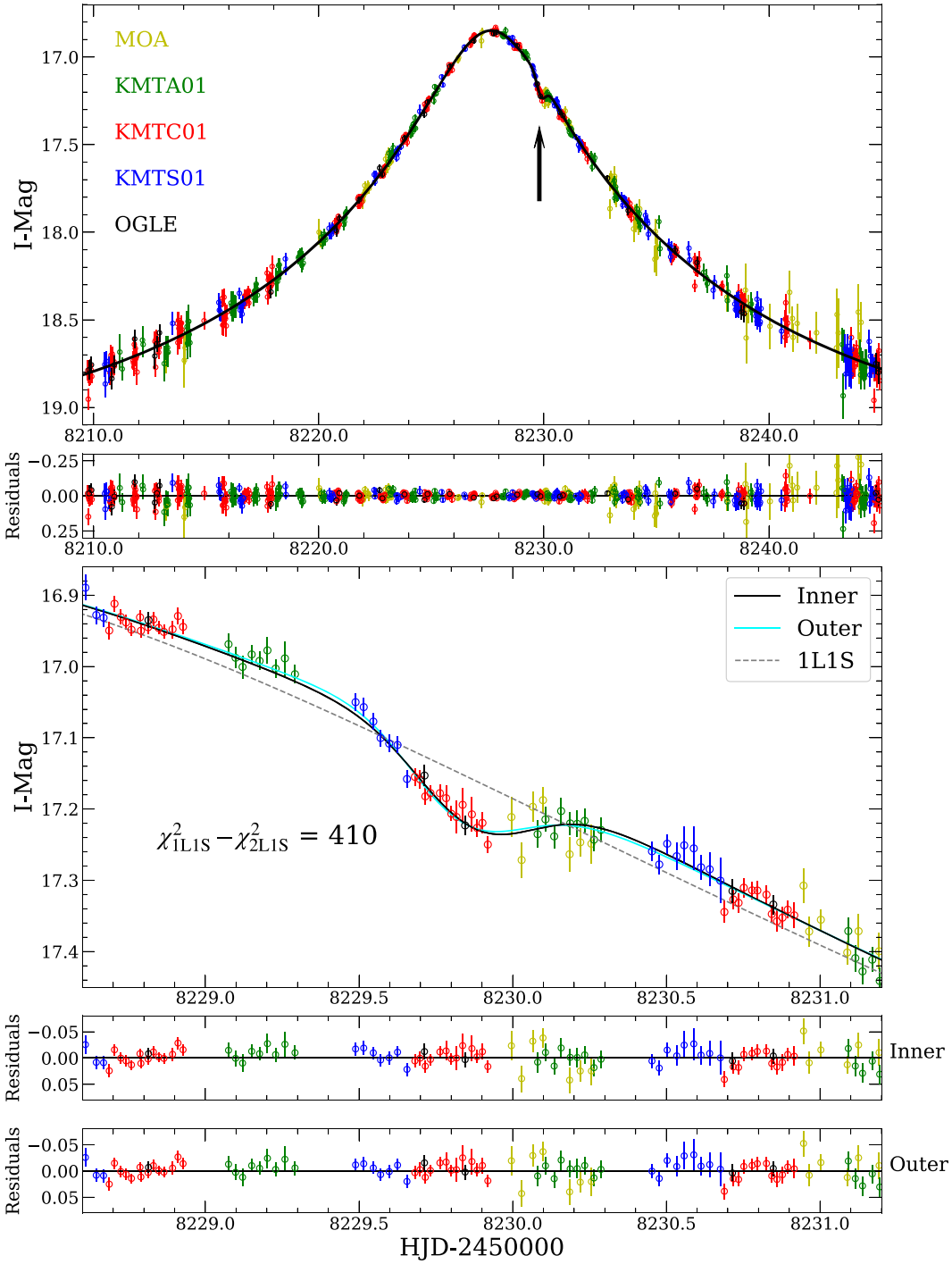

Figure 4. Light curve and models of OGLE-2018-BLG-0516. The main evidence for an anomaly comes from the dip at about 8229.85. This is confirmed by two OGLE points. The KMTA and MOA data trace the end of the dip, while the KMTS data are consistent with the beginning of the dip. The caustic topology is the same as for KMT-2019-BLG-0253 and OGLE-2018-BLG-0506. See Figure 2.

(The data used to create this figure are available.)

3.7. OGLE-2019-BLG-0953

In contrast to the previous five events, the amplitude of the anomaly (a dip at HJD$' \simeq 8643.7$, i.e., $\Delta t_{\rm anom} = +5.4$ days) is not much larger than the individual KMT error bars. See Figure 7. However, this event lies in a small (0.4 deg^2) zone that is covered by four fields and so is observed at $\Gamma = 8\,{\rm hr}^{-1}$. All four fields from two observatories (KMTC and KMTS) participate in the same overall trend during the night of the dip. Moreover, the dip is confirmed by eight OGLE points. Hence, it is secure.

3.7.1. Heuristic Analysis

The 1L1S model yields parameters $t_{\rm E} \simeq 11.5$ days and $u_0 \simeq 0.5$. We estimate $\Delta t_{\rm dip} = 0.9$ days and, as noted above, $\Delta t_{\rm anom} = 5.4$ days. Applying the heuristic formalism of

Table 6
2L1S Parameters for OGLE-2019-BLG-1492

Parameters	Static		Parallax			
	Inner	Outer	Inner $u_0 > 0$	Inner $u_0 < 0$	Outer $u_0 > 0$	Outer $u_0 < 0$
χ^2	6792.	6793.4	6789.0	6789.6	6790.2	6790.6
dof	6791	6791	6789	6789	6789	6789
t_0	8763.137	8763.142	8763.120	8763.125	8763.131	8763.129
	0.027	0.026	0.032	0.032	0.032	0.033
u_0	0.0507	0.0508	0.0473	−0.0480	0.0480	−0.0478
	0.0032	0.0031	0.0043	0.0042	0.0045	0.0042
t_E (days)	50.1	50.1	52.8	52.4	52.4	52.1
	2.7	2.7	4.2	4.0	4.1	3.9
s	0.898	1.044	0.903	0.904	1.043	1.045
	0.015	0.018	0.014	0.015	0.018	0.019
q (10^{-5})	19.1	17.6	18.0	17.8	17.3	17.6
	5.8	5.4	4.9	5.4	4.9	5.0
α (rad)	2.123	2.120	2.140	−2.135	2.134	−2.139
	0.023	0.022	0.026	0.030	0.030	0.031
ρ	<0.009	<0.009	<0.009	<0.009	<0.009	<0.009
$\pi_{E,N}$	⋯	⋯	−0.342	0.143	−0.210	0.575
	⋯	⋯	0.858	0.957	0.922	0.815
$\pi_{E,E}$	⋯	⋯	−0.062	−0.026	−0.042	−0.001
	⋯	⋯	0.093	0.102	0.106	0.108
$\pi_{E,\parallel}$	⋯	⋯	−0.047	−0.034	−0.030	−0.042
	⋯	⋯	0.085	0.088	0.092	0.091
$\pi_{E,\perp}$	⋯	⋯	0.344	−0.141	0.212	−0.573
	⋯	⋯	0.859	0.959	0.923	0.817
ψ (deg)	⋯	⋯	92.5	93.1	93.3	94.1
$I_{S,\ KMTC01}$	21.01	21.00	21.09	21.07	21.07	21.07
	0.07	0.07	0.10	0.10	0.10	0.10

Note. The upper limits on ρ are at 3σ.

Section 3.1, these yield

$$\begin{aligned} \alpha &= 137°; \quad s \simeq s_-^\dagger \pm \Delta s; \\ s_-^\dagger &= 0.71; \quad q \sim 17 \times 10^{-5}. \end{aligned} \tag{14}$$

Again, $\pm\,\Delta s$ cannot be determined at this level of analysis.

3.7.2. Static Analysis

In sharp contrast to the other four non-caustic-crossing events (all of the above except OGLE-2018-BLG-0977), the grid search described in Section 3.1 returns only one local minimum. We then further refine this by allowing all parameters to vary in the MCMC. The resulting solution is given in Table 8 and illustrated in Figure 7.

The physical reason that the inner–outer degeneracy is broken in this case can be assessed by comparing the caustic topology of KMT-2019-BLG-0953 to the other four non-caustic-crossing cases in Figure 2. For this event, the (unique) solution has the "outer" geometry, but with isolated planetary caustics, whereas in the other four cases the outer solution had a resonant caustic. Hence, if there were two solutions, they would lie on opposite sides of isolated planetary caustics. This alternate topology follows from the fact that $u_{anom} \sim 0.7$, compared to 0.07–0.13 for the other four cases, which means that it is far from the resonant regime (for low-q companions). Because minor-image isolated caustics have substantial structure in the direction perpendicular to the binary axis, the inner–outer degeneracy can usually be broken when both trajectories pass isolated caustics, unless the trajectories are themselves close to perpendicular, as in the case of OGLE-2016-BLG-1067 (Calchi Novati et al. 2019).

Because there is only one solution, $s^\dagger$ is expected to be merely offset from the (unique) value of s, rather than being nearly equal to the average of two values, as in the other four cases. Nevertheless, this offset is small: $s - s^\dagger = 0.03$, while the fitted values of both q and α are all in good agreement with Equation (14).

Note that there is only a weak constraint on the source size, ρ, which corresponds to $t_* < 0.33$ days.

3.7.3. Parallax Analysis

Similarly to several other cases, we find that the baseline data would generate a spurious parallax signal. We therefore restrict the analysis to $8600 <$ HJD$' < 8670$, i.e., roughly $t_0 \pm 3\,t_E$, which we then also apply to the static solution. After doing so, we find that the microlens parallax $\boldsymbol{\pi}_E$ is not meaningfully constrained, and we therefore adopt the static solution.

4. Source Properties

Overall, our principal objective in this section is to measure the source-star angular radius, θ_*, and then to either make measurements of or obtain lower limits on

$$\theta_E = \frac{\theta_*}{\rho}; \qquad \mu_{rel} = \frac{\theta_E}{t_E}, \tag{15}$$

depending on whether ρ is measured or itself only has an upper limit. For the first step, we use the method of Yoo et al. (2004).

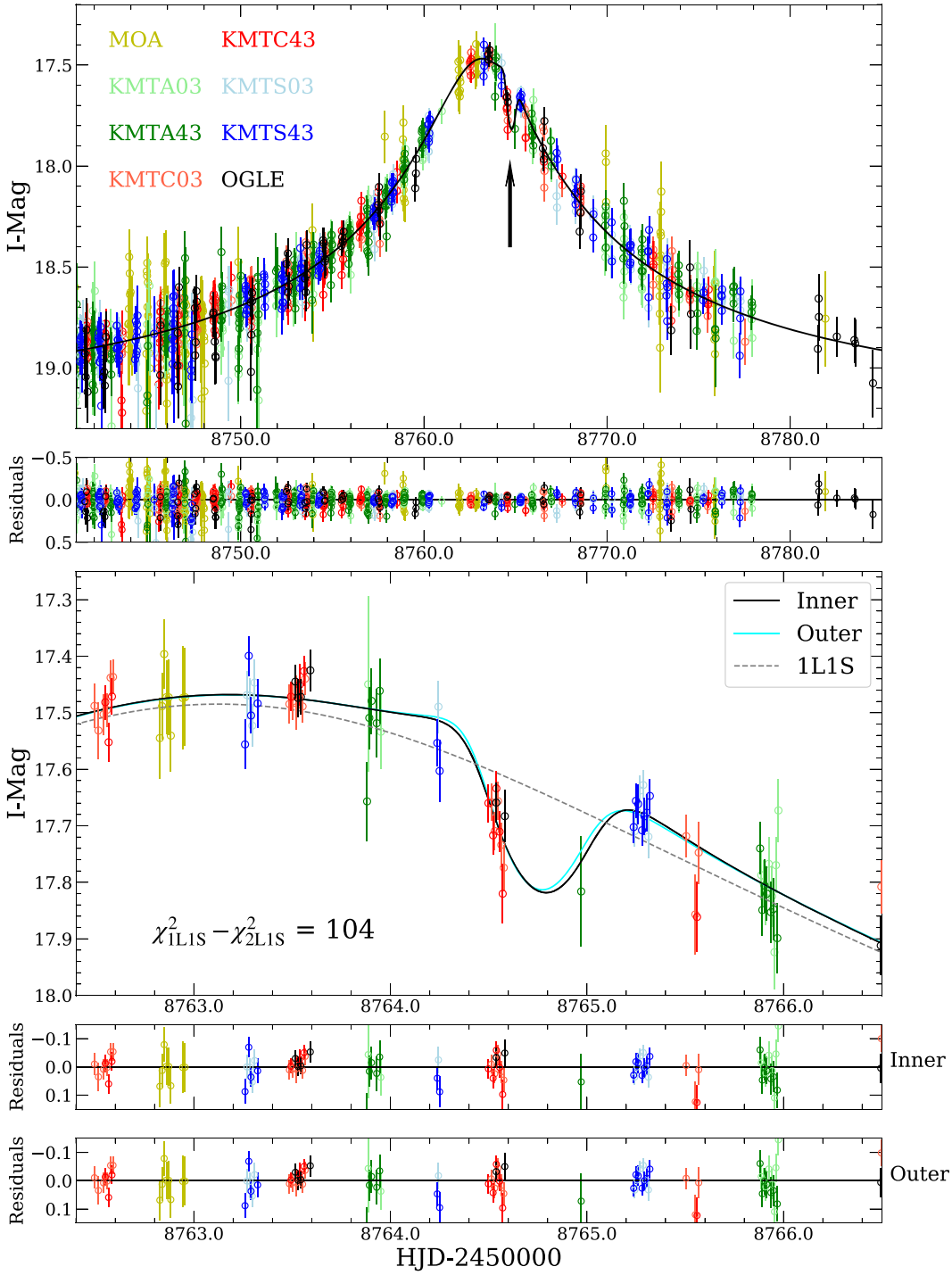

Figure 5. Light curve and models of OGLE-2019-BLG-1492. The main evidence for the anomaly comes from the dip in KMTC data at about 8764.65, which is confirmed by two OGLE points. It is also supported by the post-dip "ridge" in KMTS data at about 8665.25. The caustic topology is the same as for KMT-2019-BLG-0253, OGLE-2018-BLG-0506, and OGLE-2018-BLG-0516. See Figure 2.

(The data used to create this figure are available.)

That is, we first measure the color–magnitude offset between the source and the centroid of the red clump on a color–magnitude diagram (CMD),

$$\Delta[(V-I), I] = [(V-I), I]_s - [(V-I), I]_{\rm cl}. \quad (16)$$

Next, we adopt $(V-I)_{\rm cl,0} = 1.06$ from Bensby et al. (2013), and we evaluate $I_{\rm cl,0}$ from Table 1 of Nataf et al. (2013), based on the Galactic longitude of the event. We then find the dereddened color and magnitude of the source

$$[(V-I), I]_{\rm s,0} = [(V-I), I]_{\rm cl,0} + \Delta[(V-I), I]. \quad (17)$$

We then apply the *VIK* color–color relations of Bessell & Brett (1988) to transform from V/I to V/K, and finally, we apply the color/surface brightness relations of Kervella et al. (2004) to

Table 7
2L1S Parameters for OGLE-2018-BLG-0977

Parameter	Value	Error
χ^2/dof	1553.0/1553	
t_0	8276.600	0.018
u_0	0.1470	0.0097
t_E (days)	20.37	1.15
s	0.8793	0.0066
q (10^{-5})	4.15	0.43
α (rad)	2.5063	0.0079
ρ	<0.0033	
$I_{S,\ KMTC01}$	20.268	0.077

Note. The upper limit on ρ is at 3σ.

obtain θ_*. After propagating the measurement errors, we add 5% to the error in quadrature to take account of systematic effects in the method as a whole.

Figure 8 shows the CMDs for all six events. For one of these (OGLE-2018-BLG-0516), the CMD field stars are drawn from the pyDIA (Albrow 2017) reduction of a $2' \times 2'$ square centered on the event. The source color is determined from regression of the V-band and I-band source fluxes during the event. The source magnitude is calculated from the value in Table 5 added to the offset between the pyDIA and pySIS systems as determined by regression of their respective light curves.

For the remaining four events (KMT-2019-BLG-0253, OGLE-2018-BLG-0516, OGLE-2019-BLG-1492, and OGLE-2018-BLG-0977), the CMD field stars are drawn from the calibrated OGLE-III catalog (Szymański et al. 2011), with respective radii of 80″, 120″, 100″, and 90″. These values were chosen by balancing the competing demands of attaining sufficient density to determine the position of the clump and minimizing the effects of differential extinction. To determine the source position on the OGLE-III CMD, the same steps were first taken as for OGLE-2018-BLG-0516. Then, the pyDIA CMD was calibrated to OGLE-III, allowing the source position to be transformed.

Table 9 shows the measurements and logical train described above for all six events. In addition, we comment on specific aspects of particular events below.

4.1. KMT-2019-BLG-0253

KMT-2019-BLG-0253 has significant blended light, which raises the question of whether or not this blend could be due to the lens. The CMD position of the baseline object $[(V-I), I]_{\rm base} = (3.30,\ 18.84) \pm (0.18,\ 0.06)$ was determined by transforming the KMTC02 pyDIA field-star photometry at the position of the event to the OGLE-III system.[34] We also measured the Sloan Digital Sky Survey i flux at this position from seven images taken with CFHT in 0.″5 seeing, transformed to the OGLE-III system. This confirmed the KMTC02 $I_{\rm base}$ measurement within errors. Subtracting the source flux from the baseline flux yields the blended flux $[(V-I), I]_b = (3.67,\ 19.42) \pm (0.46,\ 0.10)$. The baseline object and blended light are shown in Figure 8 as green and magenta points, respectively.

We transform the source position (as determined from KMTC02 difference images) to the CFHT 0.″5 images and measure its offset from the baseline object, finding

$$\Delta\boldsymbol{\theta}(E, N) = \boldsymbol{\theta}_{\rm base} - \boldsymbol{\theta}_x = (-31,\ -6) \pm (7,\ 10)\,{\rm mas}. \quad (18)$$

This offset is formally inconsistent with zero at more than 4σ, which would nominally rule out the lens as the origin of the blended light. In fact, as we show below, there are physical effects that can account for this offset, even if the blended light is due to the lens.

However, first we note that this small offset can be compared with the overall surface density of field stars that are brighter than the blend, $I_b = 19.42$, which we find from the OGLE CMD to be $N = 0.012\ {\rm arcsec}^{-2}$. Taking Equation (18) at face value and noting that the blend:source flux ratio is 1.75, the separation of the source and blend is 50 mas. Thus, the probability of such a chance superposition is $p = \pi N((11/7)\Delta\theta)^2 \sim 1 \times 10^{-4}$, which is to say, virtually ruled out. Hence, the blended light is due to the lens itself, a companion to the lens, or a companion to the source.

One possibility for the offset in Equation (18), just mentioned, is that it is due to a companion to the source or the lens. For the source (at $D_S \sim 8$ kpc), the projected separation would correspond to ∼250 au. For the lens, it would be proportionately closer, e.g., ∼150 au at $D_L \sim 5$ kpc. Such $\log(P/{\rm day}) \sim 6$ stellar companions are among the most common. See Figure 7 of Duquennoy & Mayor (1991). On the other hand, if the blend were a companion to the source, it would be a subgiant, i.e., of almost identical mass to the source. From Table 7 of Duquennoy & Mayor (1991), this would be quite rare. It is more plausible that the blend is a companion to the lens, simply because there are no independent constraints on its mass ratio or distance.

However, another possibility is that an ambient star (contributing some, but not all, of the blended light) is corrupting the measurement of $\boldsymbol{\theta}_{\rm base}$. Suppose, for example, that 10% of the baseline flux were due to an ambient star at ∼300 mas from the source (and lens). This would be too faint and too close to be separately resolved, even in 500 mas seeing. Therefore, the fitting program would find the flux centroid displaced by $0.1 \times 300\ {\rm mas} = 30\ {\rm mas}$, which is what is observed. We can estimate the surface density of stars that are 2.5 ± 0.5 mag fainter than the baseline object (i.e., $M_I = 4.5 \pm 0.5$) using the Holtzman et al. (1998) luminosity function, based on Hubble Space Telescope (HST) observations of Baade's window. We must first multiply by a factor 3 based on the relative surface density of clump stars in the KMT-2019-BLG-0253 field compared to Baade's window (Nataf et al. 2013; D. Nataf 2019, private communication). We then find a surface density $N = 1.0\ {\rm arcsec}^{-2}$. Hence, the probability that one such star falls within 0.″3 of the lens is about 25%.

We conclude that the blend is most likely either the lens itself or a companion to the lens. It could be a companion to the source with much lower probability. And it is very unlikely to be an ambient star.

[34] Note that the CMD position of the baseline object is below the threshold of detection (roughly $V \sim 21.5$) on the OGLE-III CMD but still has only moderate color error in the KMT field-star photometry. This is because the V-band photometry is carried out by different methods. For OGLE-III, sources on the V and I templates are found independently and then matched based on astrometry. For KMT sources are identified only in I band. Then, the V-band measurement is derived from the V-band flux at this I-band location, averaged over all available images.

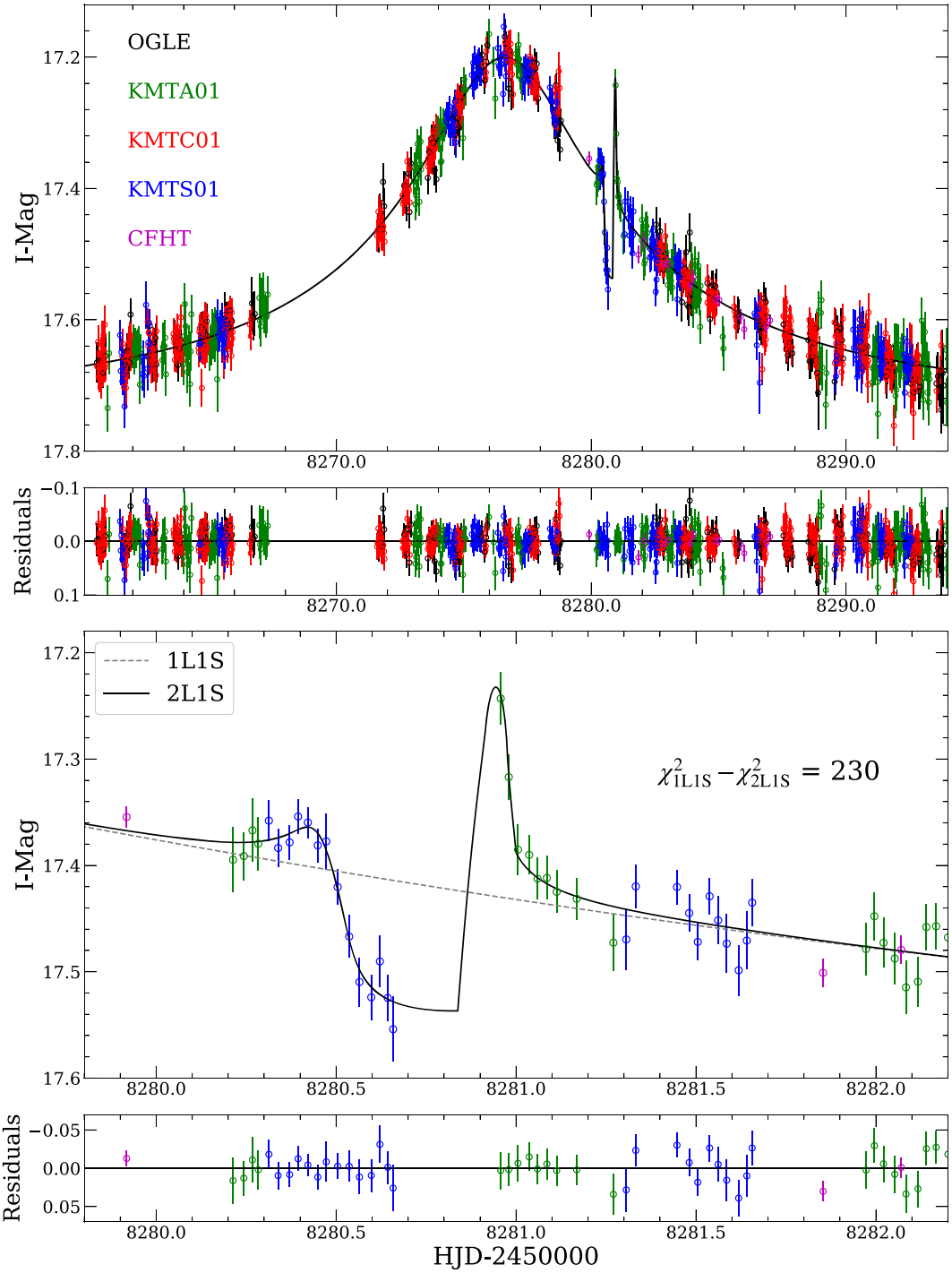

Figure 6. Light curve and model of OGLE-2018-BLG-0977. The KMTS data near 8280.5 briefly rise and then sharply fall, which indicates entrance into the trough that threads the two minor-image triangular caustics, near (but not over) one of these caustics. The KMTA data near 8281.0 show a sharp decline, followed by flattening, consistent with an exit from the triangular caustic on the opposite side of the trough. The caustic topology diagram (Figure 2) confirms this qualitative light-curve analysis.

(The data used to create this figure are available.)

4.2. OGLE-2018-BLG-0506

We note that the pyDIA reductions of the KMTC data are only approximately calibrated. However, this has no practical importance because the filters are near standard and the only quantity entering the calculations that follow is the offset between the source and the clump. Moreover, this offset is small. See Figure 8. For reference, we note that in the other four events the KMT → OGLE-III correction was found to be $[(V-I), I]_{\rm s,kmt} - [(V-I), I]_{\rm s,ogle-III} = [0.06, 0.22]$, [0.17, 0.12], [0.14, 0.01], and [0.03 ,0.22], for KMT-2019-BLG-0253, OGLE-2018-BLG-0516, OGLE-2019-BLG-1492, and OGLE-2018-BLG-0977, respectively.

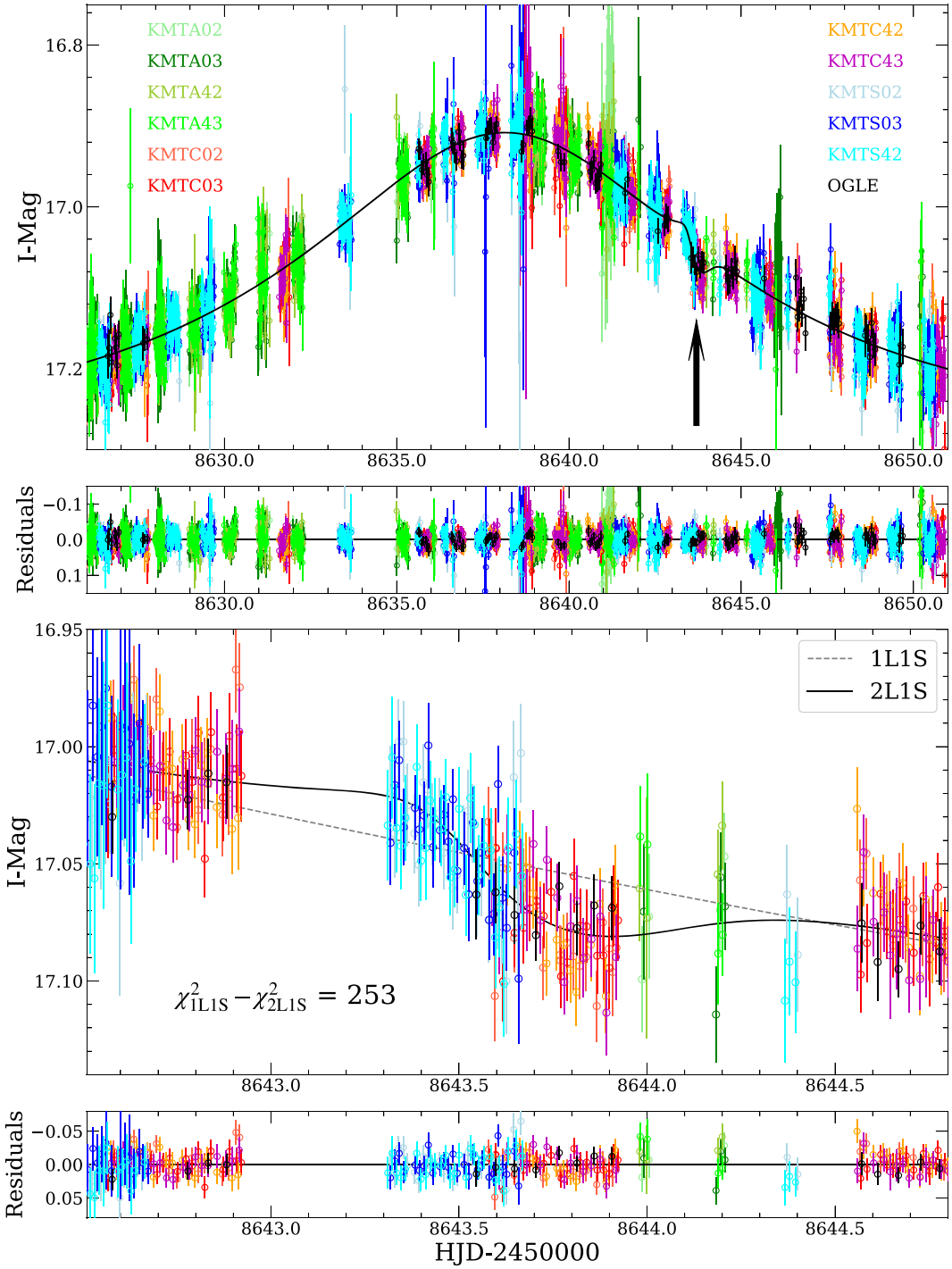

Figure 7. Light curve and model of KMT-2019-BLG-0953. The KMTS and KMTC data show a low-amplitude dip $8643.4 \lesssim \mathrm{HJD}' < 8643.9$, which is not much larger than the individual error bars, but because the event lies in a small region with very high cadence, there are >100 data points during this 12 hr interval. Eight OGLE points near the trough confirm the dip. The dip indicates that the source passed near, but not over, the minor image due to the host. See Figure 2.

(The data used to create this figure are available.)

We find a best estimate for the blended light $I_b = 21.08$ on the OGLE-IV system and $I_b = 21.11$ on the KMTC41 pyDIA system. Even ignoring the uncertainties in this estimate due to the mottled background light, which can be considerable (e.g., Gould et al. 2020), this measurement would play very little role when treated as an upper limit on lens light. For example, even at $M = 1\,M_\odot$ (the 1σ upper limit derived in Section 5) and at $D_L = 5.6$ kpc, the lens magnitude would be $I_L \sim 22.2$. Therefore, we do not pursue a detailed investigation of this blend.

4.3. OGLE-2018-BLG-0516

The KMTC01 pyDIA analysis formally yields a negative blended flux that, after conversion to the OGLE-III system,

Table 8
2L1S Parameters for KMT-2019-BLG-0953

Parameter	Value	Error
χ^2/dof	909.0/9092	
t_0	8638.149	0.015
u_0	0.491	0.023
t_E (days)	11.62	0.39
s	0.736	0.010
q (10^{-5})	17.8	3.4
α (rad)	2.3601	0.0077
ρ	<0.028	
$I_{S,\ KMTC02}$	18.474	0.078

Note. The upper limits on ρ are at 3σ.

corresponds to an $I_b = 21.1$ "anti-star." This level of negative blending would be easily explained by errors in the PSF-fitting photometry of faint stars in the baseline images, even without taking account of the unresolved mottled background. Hence, it is of no concern in itself and can be regarded as consistent with zero. The field has extinction $A_I = 1.87$. Hence, a lens with $M = 0.84\,M_\odot$ (the 1σ upper limit derived in Section 5) at $D_L \sim 7.0$ kpc would have brightness $I_L = 20.8$. This is comparable to the error in the measurement of the blended flux (as demonstrated by its negative value). Hence, no useful limits on the lens flux can be derived.

4.4. OGLE-2019-BLG-1492

For four of the six events, the position of the source on the CMD corresponds to what is expected for a reasonably common class of bulge star. These are turnoff stars (KMT-2019-BLG-0253 and OGLE-2018-BLG-0516), a clump giant (OGLE-2018-BLG-0506), and a mid-G dwarf (OGLE-2018-BLG-0977). However, the source position for OGLE-2019-BLG-1492 is somewhat puzzling and deserves further investigation.

The source has a similar color to the Sun but is about 1.45 mag fainter than the Sun would be if it were at the mean distance of the clump. This could, in principle, be resolved by it being 1.45 mag dimmer than the Sun or 1.45 mag more distant than the clump, or some combination. For example, for the first, it could be that the source is a relatively unevolved metal-poor star. Another potential explanation is that the source color has not been correctly measured. For example, if the source were 0.2 mag redder, it would be expected to be 1 mag or more dimmer than the Sun. However, the color is determined from regression of about a dozen well-magnified V-band points that lie along the regression line. Hence this explanation appears unlikely. Regardless of the exact explanation of the discrepancy, it has little practical effect. That is, even if θ_* were double the value that we have estimated in Table 9, the constraints provided by the resulting limits on θ_E and μ_{rel} would still be too weak to matter.

The blended light has $I_b = 19.47$ on the calibrated OGLE-III scale. However, the baseline V-band photometry is not precise enough to reliably determine $(V-I)_b$. In principle, this blended light might be due primarily to the lens. However, we find from CFHT baseline images in $0\farcs45$ seeing that the blend is displaced from the event by $0\farcs33$. Therefore, it cannot be the lens and so must be either a companion to the lens or to the source or an ambient star that is unrelated to the event. We find that the surface density of stars that are brighter than the blend ($I < I_b$) is 0.33 arcsec^{-2}. Thus, the probability of an ambient star within a circle of radius equal to the separation is 11%. This is the most likely explanation for the blended light.

4.5. OGLE-2018-BLG-0977

In Table 9, we only list a 3σ upper limit on ρ because the light curve is formally consistent with $\rho = 0$ at this level. However, it should be noted that at the 1σ and 2σ levels ρ is constrained by $\rho = 1.9^{+0.3}_{-0.6} \times 10^{-3}$ and $\rho = 1.9^{+0.6}_{-1.6} \times 10^{-3}$, respectively. These tighter limits on ρ result primarily from the source crossing a caustic. When evaluating the physical parameters in Section 5, we will make full use of the χ^2 fit values as a function of ρ. The blended light is a relatively bright star on the foreground main sequence $[(V-I), I]_{b,\mathrm{OGLE-III}} = (17.39, 1.98)$, which raises the possibility that this is the lens. However, we find from examining the CFHT baseline image that this blended light is a resolved star with a separation of $\sim 0\farcs5$. Thus, it is definitely not the lens, nor can it be a companion to the source. This leaves two possibilities: companion to the lens or ambient star. The surface density of foreground main-sequence stars brighter than the blend is $N = 0.0085$ arcsec^{-2}. Hence, the probability of such an ambient star within $0\farcs5$ is $p = 1/150$. This is relatively low, but the prior probability that a given star has a substantially more massive companion at separation $a_\perp \gtrsim 1000$–2000 au (for distance 2–4 kpc) is also of order 1% or less. Thus, no information about the lens system can be inferred from the presence of this bright blend.

4.6. KMT-2019-BLG-0953

There was significant difficulty measuring the source color of KMT-2019-BLG-0953. As with the other four events that lie in the OGLE-III catalog (Szymański et al. 2011) footprint, our approach is to first measure the source color in the KMT system by regression and then to transform this color to the OGLE-III system by comparison of field stars. The results for all events are shown as blue points in Figure 8. However, for KMT-2019-BLG-0953, we applied this procedure five times, using the independent data sets from KMTC02, KMTC42, KMTC03, KMTC43, and KMTS02. Strikingly, these five determinations are composed of two groups: (KMTC02, KMTC43) were closely grouped near $(V-I)_{s,\mathrm{OGLE-III}} \simeq 1.94$, while (KMTC03, KMTC42, KMTS02) were closely grouped near $(V-I)_{s,\mathrm{OGLE-III}} \simeq 2.05$. The errors in each case were near 0.04. One approach would simply be to take the average of these five measurements, which would yield a mean and standard error of the mean of 2.006 ± 0.018. This joint fit has $\chi^2 = 9.1$ for 4 dof, which has a Gaussian probability of $p = (1 + \chi^2/2)\exp(-\chi^2/2) = 6\%$. Under normal circumstances, this value would not be low enough to raise serious concerns.

However, there are two further issues that must be taken into account. First, using the clump centroid from Table 9, this would lead to a dereddened source color $(V-I)_{s,0} = 0.51 \pm 0.02$. Such blue stars are extremely rare in the bulge. Given that the source is 2.3 mag below the clump, it would have to be either a blue straggler or a relatively young star. Alternatively, it could be an F dwarf in the disk, relatively close to the Galactic bulge. This would also be unexpected.

The second issue is that the color measurement may be impacted by the presence of a bright neighbor at $1\farcs0$, which is about 2 mag brighter than the source. DIA works by first subtracting the reference image convolved with a kernel and

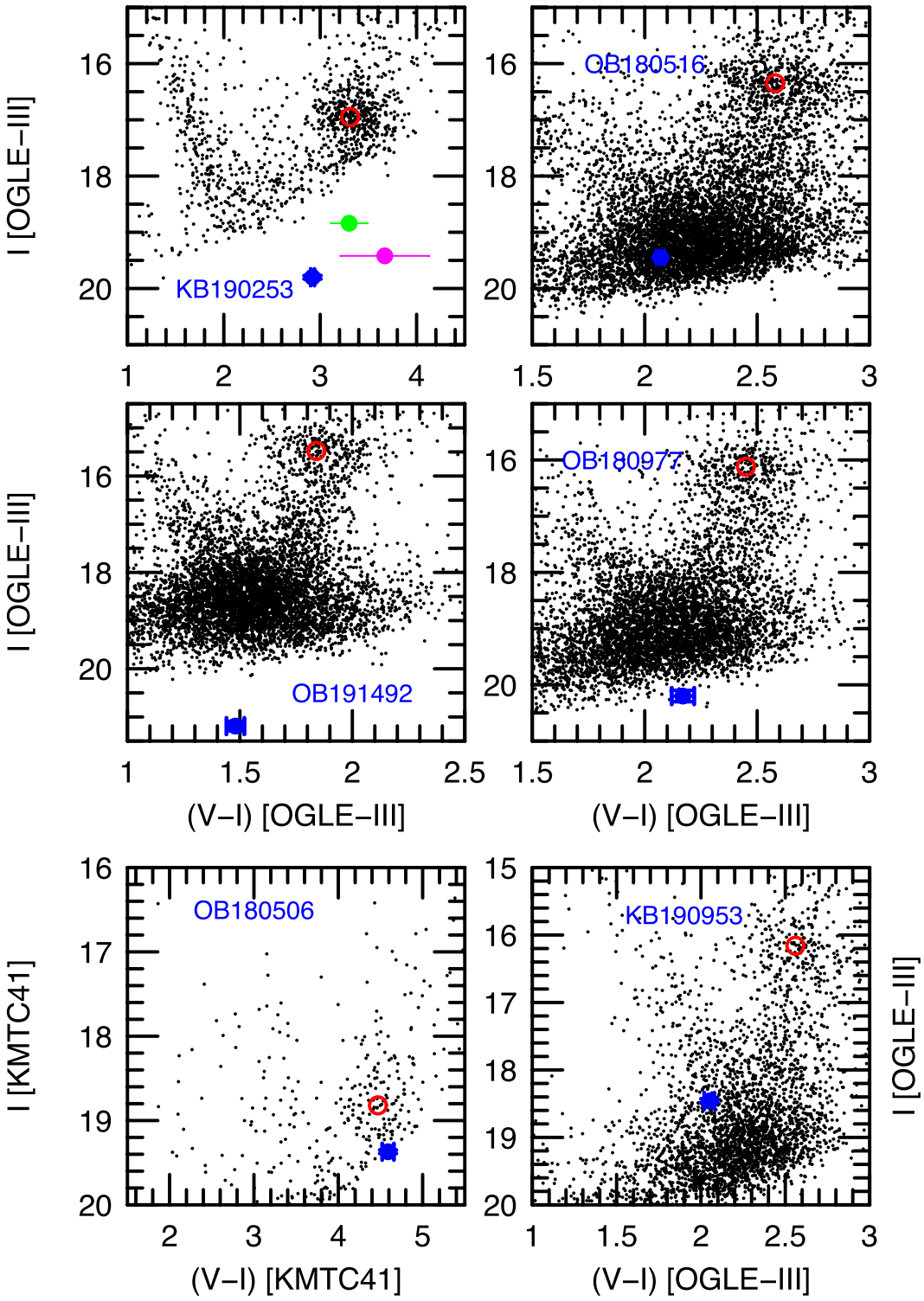

Figure 8. CMDs for each of the six $q < 2 \times 10^{-4}$ planets reported here. The source positions (blue) and clump-giant centroids (red) are shown for all events. For KMT-2019-BLG-0253, the baseline object (green) and blended light (magenta) are also shown. Photometry is in the calibrated OGLE-III system for all except OGLE-2018-BLG-0506 (lower left), which is in the KMTC41 pyDIA system.

then multiplying the resulting difference image by the point-spread function (PSF). If the subtraction were perfect, the only impact of the neighbor would be to add photon noise, which is already taken into account in the measurement process. However, the PSF varies over the field, particularly near the edge of the field (recall that this event lies in the overlap of two neighboring fields), so that the PSF and resulting kernel are inevitably less than perfect. Then, residuals from an imperfectly subtracted, bright, overlapping neighbor can impact the photometry. Thus, the difficulties induced by this neighbor

Table 9
CMD Parameters for Six $q < 2 \times 10^{-4}$ Events

Parameter	KB190253	OB180506	OB180516	OB191492	OB180977	KB190953
$(V-I)_s$	2.92 ± 0.01	4.59 ± 0.07	2.07 ± 0.02	1.48 ± 0.04	2.17 ± 0.05	2.05 ± 0.04
$(V-I)_{cl}$	3.31 ± 0.02	4.47 ± 0.02	2.58 ± 0.02	1.84 ± 0.02	2.45 ± 0.03	2.56 ± 0.03
$(V-I)_{cl,0}$	1.06	1.06	1.06	1.06	1.06	1.06
$(V-I)_{s,0}$	0.67±0.03	1.18 ± 15.10	0.55 ± 0.03	0.70 ± 0.05	0.78 ± 0.05	0.55 ± 0.05
I_s	19.80 ± 0.02	19.37 ± 0.02	19.45 ± 0.02	21.10 ± 0.10	20.20 ± 0.08	18.46 ± 0.08
I_{cl}	16.95 ± 0.03	18.82 ± 0.04	16.35±00.03	15.40 ± 0.04	16.12 ± 0.03	16.16 ± 0.03
$I_{cl,0}$	14.44	14.55	14.48	14.38	14.47	14.38
$I_{s,0}$	17.29 ± 0.03	15.10 ± 0.05	17.58 ± 0.04	20.08 ± 0.11	18.55 ± 0.10	16.68 ± 0.09
θ_* (μas)	1.05 ± 0.07	5.11 ± 0.35	0.81 ± 0.05	0.30 ± 0.04	0.66 ± 0.08	1.22 ± 0.08
θ_E (mas)	>0.23	>0.43	>0.08	>0.03	>0.20	>0.044
μ_{rel} (mas yr^{-1})	>1.5	>6.5	>1.1	>0.2	>3.6	>1.4

Note. Event names are abbreviations for, e.g., OGLE-2018-BLG-0506 and KMT-2019-BLG-0253. Lower limits on θ_E and μ_{rel} are 3σ.

might plausibly account for the relatively high χ^2/dof of the joint fit, in which case the high scatter would be due to systematics, so that the errors could not be treated as Gaussian.

We resolve these challenges as follows. First, we derive the color from the three redder measurements and ignore the two bluer measurements as plausibly due to systematics. Second, we adopt the standard deviations of these measurements, rather than the standard error of the mean, in order to reflect the non-Gaussian errors. Third, with these assumptions, the source is very plausibly a bulge star, and so we assign it bulge kinematics in the Bayesian analysis of Section 5.

However, we also briefly discuss the implications for both present and future work, if the source is later proved by follow-up observations to be bluer than we have assumed.

First, such a bluer source would yield a smaller θ_*. In particular, it would be ~10% smaller if the source were 0.11 mag bluer. Under normal circumstances, this would affect the Bayesian estimates by reducing both θ_E and μ_{rel} by 10%. However, in the present case, we have only weak lower limits on these quantities (see Table 9), so there is essentially no impact. Furthermore, if the lens and source are separately resolved by future adaptive optics (AO) observations, then μ_{rel} (and so $\theta_E = \mu_{rel} t_E$) will be directly determined from these observations, so that the current θ_* estimate will become moot.

The main impact would be that a blue source would almost certainly imply that the source is in the disk, which then implies that the lens (which must lie in front of the source) is also in the disk. Thus, adopting a blue color would affect the Bayesian estimates. The error bars of these estimates are already quite large, and we regard the probability of a blue source to be sufficiently small to ignore this possibility. Hence, the main role of this section will be to alert workers carrying out future follow-up observations to the difficulties of the color measurement, so that they can properly take these into account in their analyses.

5. Physical Parameters

When both θ_E and π_E are measured, one can directly determine the lens mass and lens−source relative parallax by inverting Equation (7), and one can then infer the lens distance D_L by estimating the source parallax π_S, which also yields an estimate of the projected planet-host separation, $a_\perp$,

$$M = \frac{\theta_E}{\kappa \pi_E}; \quad D_L = \frac{\mathrm{au}}{\theta_E \pi_E + \pi_S};$$
$$a_\perp = \frac{s}{\pi_E + \pi_S/\theta_E}\mathrm{au}. \tag{19}$$

Unfortunately, we do not measure both θ_E and π_E for any of the six events. For four of the six events we obtain a constraint on $\boldsymbol{\pi}_E$ (a "one-dimensional parallax" measurement), while for the other two (OGLE-2018-BLG-0977 and KMT-2019-BLG-0953) we do not obtain any constraint of $\boldsymbol{\pi}_E$. For each of the six events, we obtain only a constraint on ρ (and so on $\theta_E = \theta_*/\rho$). We therefore must estimate the physical parameters from a Bayesian analysis using Galactic model priors.

We apply the procedures of Paper I to each of the six planetary events. In each case, we consider an ensemble of simulated events drawn from a Galactic model. We weight these events by the product of five terms,

$$\Gamma \propto \theta_E \mu_{rel} \chi^2(t_E) \chi^2(\boldsymbol{\pi}_E) \chi^2(\rho). \tag{20}$$

The first two terms are simply the cross section and speed from the very general rate formula "$\Gamma = n\sigma v$." The third term reflects how well the Einstein timescale of the simulated event matches that of the actual event, within the latter's measurement error. Similarly, the fourth term reflects the match of $\boldsymbol{\pi}_E$ between the simulated and observed events. The only difference is that, because $\boldsymbol{\pi}_E$ is a two-dimensional (2D) quantity, the comparison is made via a 2D error ellipse rather than a 1D error bar. For OGLE-2018-BLG-0977 and KMT-2019-BLG-0953, the best value of t_E and its error bar come from Table 7. For the remaining four events, the parallax values and error ellipses come from ($\pi_{E,\parallel}$, $\pi_{E,\perp}$, ψ) in Tables 3–6, while the t_E and error bars come from the corresponding solutions.

The only element of Equation (20) that is somewhat less familiar is $\chi^2(\rho)$. Normally, one measures ρ and infers $\theta_E = \theta_*/\rho$ (with some error bar), and so this term is usually expressed in the form $\chi^2(\theta_E)$. However, lacking ρ measurements, we proceed as follows.

From the MCMC, we evaluate the lower envelope of χ^2 as a function of ρ. For example, for the case of KMT-2019-BLG-0253, this is similar to a Heaviside step function, e.g., $\chi^2(\rho) = 100\Theta(0.0035)$, in which any value $\rho < 0.0035$ would

Table 10
Bayesian Estimates of Physical Parameters

Event Name	$M_{\rm host}$ ($M_\odot$)	$M_{\rm planet}$ ($M_\oplus$)	D_L (kpc)	$a_\perp$ (au)	$\mu_{\rm rel}$ (mas)
KMT-2019-BLG-0253	$0.70^{+0.34}_{-0.31}$	$9.2^{+5.0}_{-4.1}$	$4.9^{+1.9}_{-1.6}$	$3.1^{+0.8}_{-0.9}$	$4.7^{+2.8}_{-2.1}$
OGLE-2018-BLG-0506	$0.63^{+0.37}_{-0.32}$	$16.3^{+12.0}_{-8.5}$	$5.6^{+1.4}_{-1.6}$	$3.0^{+0.7}_{-0.8}$	$8.1^{+2.5}_{-1.5}$
OGLE-2018-BLG-0516	$0.47^{+0.38}_{-0.25}$	$20.1^{+16.4}_{-10.7}$	$7.0^{+0.9}_{-2.2}$	$2.2^{+0.8}_{-0.7}$	$5.0^{+2.9}_{-1.9}$
OGLE-2019-BLG-1492	$0.68^{+0.34}_{-0.34}$	$37.1^{+25.1}_{-19.5}$	$5.6^{+1.7}_{-2.2}$	$2.7^{+0.9}_{-0.9}$	$3.8^{+3.2}_{-1.7}$
OGLE-2018-BLG-0977	$0.47^{+0.38}_{-0.27}$	$6.4^{+5.2}_{-3.7}$	$6.5^{+1.2}_{-2.2}$	$2.0^{+0.6}_{-0.5}$	$6.9^{+3.0}_{-1.8}$
KMT-2019-BLG-0953	$0.28^{+0.32}_{-0.17}$	$15.5^{+19.0}_{-9.7}$	$7.2^{+0.7}_{-1.4}$	$1.1^{+0.5}_{-0.4}$	$7.0^{+3.3}_{-2.5}$

be permitted with no χ^2 penalty, and all others would be strictly excluded. By contrast, for the case of OGLE-2018-BLG-0977, $\chi^2(\rho)$ has a clear minimum at $\rho \sim 0.0019$, i.e., well below the 3σ limit $\rho < 0.0031$. However, even $\rho = 0$ is formally disfavored at only the $\sim 2\sigma$ level.

For each simulated event, i, we evaluate $\rho_i = \theta_*/\theta_{{\rm E},i}$, where θ_* is the value determined in Section 4 and $\theta_{{\rm E},i}$ is the Einstein radius of the simulated event.

For all the events except OGLE-2018-BLG-0977 and KMT-2019-BLG-0953, there are multiple solutions. For these cases, we combine the results from the different solutions, with the simulated events from each solution weighted by the $\Delta\chi^2$ (as given in Tables 3–8) for that solution. Table 10 shows the results. For more details on the Bayesian method, see Paper I.

In Section 4.1, we assessed that blended light in KMT-2019-BLG-0253 (magenta point in Figure 8) was most likely due to the lens itself or a companion to the lens. In either case, it would be at the distance to the lens, which, from Table 10, corresponds to distance modulus $(m - M) \simeq 13.45 \pm 0.75$. The blend lies 2.47 ± 0.10 mag below the clump, which has $I_{\rm cl,0} = 14.44$. At $D_L \sim 5$ kpc, the lens is almost certainly behind essentially all the dust. Thus, if the blend is either the lens or its companion, then its absolute magnitude is $M_{I,\rm bl} = 3.46 \pm 0.75$. This range is somewhat too luminous for a middle K dwarf, which is indicated by the blend's dereddened color being somewhat redder than the clump. On the other hand, a K dwarf would be quite consistent with the mass range shown in Table 10. One possibility that would account for all the constraints would be that the lens is part of a roughly equal-mass K-dwarf binary. Alternatively, the lens could be somewhat closer than indicated by the 1σ Bayesian range, in which case it would be intrinsically dimmer (at the same observed brightness). These issues can only be resolved by AO follow-up observations. In many cases, fruitful AO observations must wait for the lens and source to move apart sufficiently to permit them to be separately resolved, and for this event the time required for such separation is highly uncertain because there is only a lower limit on $\mu_{\rm rel}$. However, in the present case, immediate AO observations would be highly informative because the blend is brighter than the source, and the observations would allow one to confirm (or rule out) the conjecture that the astrometric offset observed from the ground was due to low-level contamination by an ambient star.

In Section 3.1, we argued that 1D parallax measurements can play a role in constraining the Bayesian estimates of the physical parameters, even when the χ^2 improvement is small (or even zero). We illustrate that impact in the present case by repeating the Bayesian analysis without the parallax constraint and reporting the resulting mass estimates for the first four events in Table 10: $M_{\rm host} = (0.63^{+0.38}_{-0.34}, 0.53^{+0.41}_{-0.30}, 0.42^{+0.40}_{-0.26}, 0.58^{+0.40}_{-0.33}) M_\odot$. Thus, by including the parallax constraint, the mass estimates were changed by (+11%, +19%, +12%, +21%), which is notable but below 1σ in all cases. This is not surprising given that the fractional Bayesian ranges $\delta_M \equiv (M_{+1\sigma} - M_{-1\sigma})/2M_{\rm median}$ in Table 10 are relatively large: $\delta_{M,\rm parallax} = (0.46, 0.56, 0.78, 0.50)$. However, another important impact is that these fractional ranges are themselves reduced by including the parallax constraint: $\delta_{M,\rm parallax}/\delta_{M,\rm static} = (0.81,\ 0.84,\ 0.99,\ 0.79)$. That is, the fractional range was substantially reduced in all but one case.

6. Discussion

We have applied the method of Paper I to the six KMT prime fields (BLG01/02/03/41/42/43) for the 2018–2019 seasons, with the aim of obtaining a homogeneously selected sample of planets with $q < 2 \times 10^{-4}$. Specifically, we obtained TLC reductions of all events that had $q < 3 \times 10^{-4}$ based on pipeline reductions, and we thoroughly investigated these events using the TLC reductions. While a full analysis must await the further application of this method to more seasons (at least 2016–2017) and more fields, it is of considerable interest to review the properties of this initial sample.

Table 11 shows all the previously known planets that were recovered by our approach, regardless of q. Table 12 shows the 11 events with planets $q < 2 \times 10^{-4}$ (7 discovered and 4 recovered) by our approach, rank ordered by $\Delta\chi^2_0$ of anomaly detection (see Paper I). A striking feature of this table is that all the new discoveries are at the top, i.e., they all have lower $\Delta\chi^2_0$ than any of the recoveries. This implies that, broadly speaking, machine selection of anomaly candidates is more robust than by-eye selection. Of course, it is still necessary for humans to vet these candidates, whether initially selected by machine or by eye.

In fact, there are two exceptions to this pattern that are not reflected in Table 12. First, OGLE-2018-BLG-0677Lb (Herrera-Martin et al. 2020), with $q = 9.1 \times 10^{-5}$, was not found by our approach because it was below our $\Delta\chi^2_0 = 75$ threshold, yet it was found by eye. Second, KMT-2018-BLG-1025Lb (Han et al. 2021d), with $q_{\rm best} = 8 \times 10^{-5}$, is not shown in Table 12 because it has a second solution at $q = 16 \times 10^{-5}$, with $\Delta\chi^2 = 8.4$, and so it is not suitable for investigating the mass-ratio function. Nevertheless, because it was recovered at $\Delta\chi^2_0 = 140$, it would break the simple pattern of Table 12 if it were included. Both examples show that humans are competitive with machines in some individual cases. Nevertheless, the overall message from Table 12 remains the same: many subtle planetary signatures escape recognition in by-eye searches. Note also from Table 12 that $\Delta\chi^2_0$ is hardly correlated with q, if at all.

Table 11
Recovered Planets in KMT Prime Fields for 2018–2019

Event Name	KMT Name	$\log q$	s	Reference
OB181185	KB181024	−4.17	0.96	Kondo et al. (2021)
KB181025[a]	KB181025	−4.03	0.95	Han et al. (2021d)
OB180532	KB181161	−4.01	1.01	Ryu et al. (2020)
OB180596	KB180945	−3.74	0.51	Jung et al. (2019a)
OB181269	KB182418	−3.24	1.12	Jung et al. (2020a)
OB180932	KB182087	−3.15	0.74	in prep
OB180567	KB180890	−2.91	1.81	Jung et al. (2021)
KB180748	KB180748	−2.69	0.94	Han et al. (2020c)
OB180962	KB182071	−2.62	1.25	Jung et al. (2021)
OB180100[a]	KB182296	−2.58	1.30	in prep
OB181011[b,c]	KB182122	−2.02	0.75	Han et al. (2019)
OB181700[b]	KB182330	−2.00	1.01	Han et al. (2020b)
OB181647[b]	KB182060	−1.95	1.27	in prep
OB181011[c]	KB182122	−1.82	0.58	Han et al. (2019)
OB181544	KB180787	−1.60	0.50	Han et al. in prep
KB190842	KB190842	−4.39	0.98	Jung et al. (2020b)
KB191953[d]	KB191953	−2.72	2.30	Han et al. (2020a)
OB191180	KB191912	−2.28	1.90	Chung et al. in prep
KB191552	KB191552	−2.17	0.74	in prep
OB190954	KB193289	−1.77	0.74	Han et al. (2021b)
KB193301	KB193301	−1.40	1.47	Han et al. in prep
OB190825[a]	KB191389	−1.23	0.17	Sato et al. in prep
KB190371[e]	KB190371	−1.10	0.83	Kim et al. (2021)

Note. Event names are abbreviations for, e.g., OGLE-2018-BLG-1185 and KMT-2018-BLG-1024. All (s,q) from "in prep" events should be regarded as preliminary. *a*: large q degeneracy at $\Delta\chi^2 < 10$, or very large q error. *b*: s degeneracy. *c*: Two-planet system. *d*: identified as FSPL, but not investigated to find planet. *e*: inner/outer degeneracy; with factor 1.5 higher q.

Table 12
$\Delta\chi^2_0$ for $q < 2 \times 10^{-4}$ Sample Planets

Event Name	KMT Name	$\Delta\chi^2_0$	$\log q$	Method
OB191492	KB193004	87	−3.75	Discovery
OB180977	KB180728	117	−4.38	Discovery
OB180506	KB180835	163	−4.09	Discovery
OB180516	KB180808	197	−3.93	Discovery
KB190253	KB190253	260	−4.39	Discovery
KB190953	KB190953	283	−3.75	Discovery
OB191053	KB191504	302	−4.90	Discovery
KB190842	KB190842	585	−4.39	Recovery
OB181185	KB181024	945	−4.17	Recovery
OB180596	KB180945	1828	−3.74	Recovery
OB180532	KB181161	7657	−4.01	Recovery

Note. Event names are abbreviations for, e.g., OGLE-2018-BLG-1185 and KMT-2018-BLG-1024.

6.1. Eleven Discovered/Recovered $q < 2 \times 10^{-4}$ Planets

Our approach yielded a total of 11 planets with $q < 2 \times 10^{-4}$ in the KMT prime fields during 2018–2019, including OGLE-2019-BLG-1053Lb (which was reported in Paper I), the six reported here, and four previously discovered planets:[35] OGLE-2018-BLG-0532Lb (Ryu et al. 2020), OGLE-2018-BLG-0596Lb (Jung et al. 2019a), OGLE-2018-BLG-1185Lb (Kondo et al. 2021), and KMT-2019-BLG-0842Lb (Jung et al. 2020b).

There are four known $q < 2 \times 10^{-4}$ planets from 2018–2019 that were not found in this search: KMT-2018-BLG-0029Lb (Gould et al. 2020), OGLE-2019-BLG-0960Lb (Yee et al. 2021), KMT-2018-BLG-1988Lb (Han et al. 2021a), and OGLE-2018-BLG-0677Lb (Herrera-Martin et al. 2020). The first three of these do not lie in prime fields, while the last failed our $\Delta\chi^2_0 > 75$ cut in the initial automated anomaly search. Note that KMT-2018-BLG-1988Lb has a very large (factor 2) 1σ error in q, so that it will almost certainly not be included in mass-ratio studies.

Finally, although it is not directly germane to the present study, we note that our approach failed to recover (or fully recover) three known planets with $q > 2 \times 10^{-4}$. The first is KMT-2019-BLG-1715LABb (Han et al. 2021c), which is a 3L2S event. The automated AnomalyFinder identified the anomaly generated by the $q_2 = 0.25$ binary companion, which dominated (and so suppressed recognition of) the planetary companion $q_3 = 4 \times 10^{-3}$. The AnomalyFinder would have to be modified to take account of the possibility of planet-binary systems to have detected this planet. The second case is that of KMT-2019-BLG-1953Lb (Han et al. 2020a), which is a $q \sim 2 \times 10^{-3}$ "buried planet" (Dong et al. 2009), i.e., its signature is submerged in the finite-source effects near the peak of a high-magnification event, $A_{\rm max} \sim 1000$. It was identified in our search as a finite-source-point-lens (FSPL) anomaly. In principle, all such events should be systematically searched for planets because of their overall strong sensitivity, particularly to Jovian mass-ratio planets. However, this stage was not pursued in the present context because of the weak sensitivity of such events to very low q planets, which is the focus of the present effort.

The third case is OGLE-2018-BLG-1011Lb,c (Han et al. 2019). This is a two-planet system for which the AnomalyFinder reports a single anomaly that contains both planets. However, in contrast to the case of the binary+planet system KMT-2019-BLG-1715LABb that was mentioned above, this is not really a shortcoming. That is, the AnomalyFinder identifies the principal anomaly but does not itself classify the anomaly as "planetary" or "binary." Rather, the operator must make the decision that an anomaly is "potentially planetary." All such events must be thoroughly investigated before they can be published, and such detailed investigations, which are carried out using TLC reductions, are far more sensitive to multiplicity of planets than any potential machine search based on pipeline reductions. By contrast, the detection of a binary system will not, of itself, trigger such a detailed investigation. Because OGLE-2018-BLG-1011 was a well-known planetary system at the time that the AnomalyFinder was run on 2018 data, no investigation was needed. However, it would have been triggered if the planets were not already known.

For completeness, we note that all three of these planetary events, i.e., OGLE-2018-BLG-1011, KMT-2019-BLG-1715, and KMT-2019-BLG-1953, were designated as "anomalous" by the AnomalyFinder. However, because there were multiple anomalies in the three cases (either a third body or finite-source effects that dominated over the planet), the AnomalyFinder did not identify all of the *planetary* anomalies.

The cumulative mass-ratio distribution of these 11 planets is presented in Figure 9, which shows that they span the range $-5 < \log q < -3.7$. We have not yet measured the efficiency

[35] Not including KMT-2018-BLG-1025Lb (Han et al. 2021d), which, as mentioned above, is excluded from the sample because it has two degenerate solutions that are well separated in q.

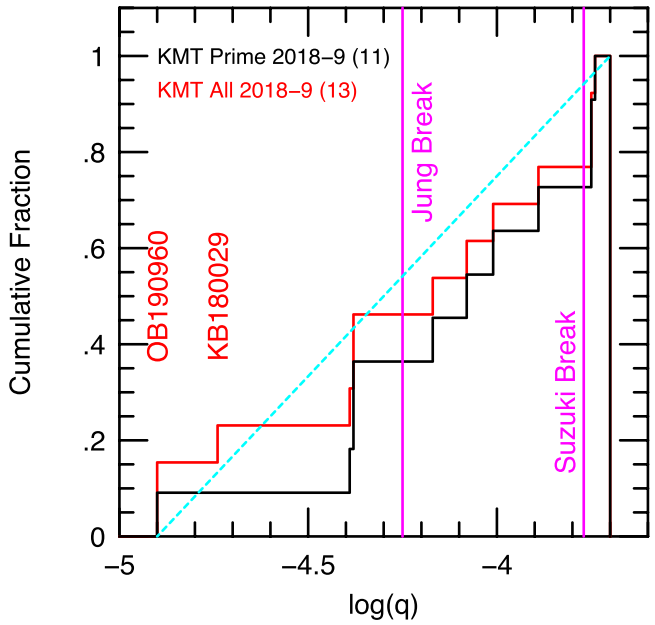

Figure 9. Cumulative distribution of recovered and discovered KMT prime-field planets from 2018–2019 (black) compared to the mass-ratio function breaks proposed by Suzuki et al. (2016) and Jung et al. (2019b; magenta). The cyan dashed line simply connects the first and last KMT detections. If the underlying distribution of mass ratios (after multiplying by the detection efficiency) were uniform in $\log q$, the cumulative distribution would approximately follow this line. The red event names at left indicate the mass ratios of the only known $q < 2 \times 10^{-4}$ planets from 2018–2019 nonprime fields. If no other such planets are found when the AnomalyFinder is applied to these fields, the cumulative distribution will be as shown in red.

of our selection, but the automatic selection should be less sensitive to lower-q planets.

In particular, the sensitivity $\xi(q)$ of any wide-angle ground-based survey that depends primarily on a χ^2 threshold to detect planets will be approximately a power law, which gradually steepens toward lower q. First, in the regime where the size of the sources (dominated by upper-main-sequence and turnoff stars) is smaller than the caustic size, the cross section for the source to interact with the caustics, or with the magnification structures that extend from them, scales as either $q^{1/2}$ or $q^{1/3}$ for planetary and resonant caustics, respectively. Second, as q falls, the duration of the anomaly declines according to the same power laws, which for fixed source brightness I_s proportionately reduces χ^2. Hence, for otherwise-similar events, the χ^2 threshold restricts lower-q planets to the brighter end of the luminosity function. Thus, if the luminosity function were a strict power law (as it roughly is for $0.5 < M_I < 3$; Figure 5 of Holtzman et al. 1998), then the efficiency would also be a power law, $\xi(q) \propto q^{\gamma}$. In fact, the luminosity becomes much shallower for $M_I \gtrsim 3$, which makes $\xi(q)$ become gradually shallower toward higher q. Finally, for low mass ratios ($\log q \lesssim -4$) where turnoff sources become comparable to or larger than the caustic size, two new effects take hold. The first is that the cross section of interaction is fixed by the source size, rather than declining with q as the caustic size. By itself, this would make the slope shallower toward lower q. However, the second effect is that the flux deviation due to the caustic is washed out by the extended source, which at fixed I_s reduces χ^2 and so restricts detections to the brighter end of the luminosity function, i.e., more so than for the case analyzed above of small sources. The net effect is to maintain a steepening $\xi(q)$ in this regime. A corollary of this logic is that if one overestimates (or underestimates) the source sizes in the efficiency calculation, then one will derive a $\xi(q)$ that is too steep (or too shallow) in the $\log q \lesssim -4$ regime. However, Figure 7 of Suzuki et al. (2016) shows that this is a relatively modest effect.

Therefore, while no rigorous conclusions can yet be drawn, a declining sensitivity function suggests that the low mass-ratio planets in this homogeneously selected sample represents a substantial underlying population. This raises questions about the previously inferred paucity of planets at low q (Suzuki et al. 2016; Jung et al. 2019b).

We note that it is already known that the low-q 2018–2019 planets KMT-2018-BLG-0029Lb ($\log q = -4.74$) and OGLE-2019-BLG-0960Lb ($\log q = -4.90$) will be recovered when we apply our approach to the nonprime KMT fields. See Figure 9. While we cannot include these in the homogeneously selected distribution because we do not yet know what new planets will be discovered in the nonprime fields, these detections prove that such planets exist. So, it will not be the case that only larger mass-ratio planets are found in these fields. Therefore, it would require many such discoveries with $\log q \gtrsim -4.3$ to maintain a strong case for a mass-ratio function that declines with declining q in the $q < 2 \times 10^{-4}$ regime. We briefly discuss the reasons that we do not consider this to be likely in Section 6.3.

6.2. Angular Distribution

An interesting difference between the recovered and discovered low-q planets is that the former all have source trajectories that are closer to the planet-host axis than the latter. The two groups have angular offsets (6°, 8°, 15°, 27°) and (31°, 36°, 45°, 50°, 58°, 59°, 74°), respectively. In particular, the two $q < 10^{-4}$ recovered planets have trajectories very close to the planet-host axis (6° and 8°). Although we have excluded KMT-2018-BLG-1025, we note that if the favored $q < 10^{-4}$ solution is indeed correct, then it also has a source trajectory close to the binary axis (5°). This probably means that it is much easier to spot by eye the extended anomalies due to such oblique encounters, compared to the short dips or bumps in the events containing the newly discovered planets. This higher sensitivity of oblique trajectories was already noted by Jung et al. (2020b), Yee et al. (2021), and Zang et al. (2021a).

6.3. Sensitivity as a Function of Γ

It is overall less likely that the seven newly discovered (as opposed to recovered) planets would have been discovered if exactly the same event had occurred in lower-cadence fields. All seven planets were *newly* discovered because a short-lived, low-amplitude perturbation was densely covered in the prime fields. Their short duration and low amplitude severely diminished[36] the chance that they would be noticed in by-eye searches, while their dense coverage enabled relatively high $\Delta\chi^2_0$ during the small, short deviation. The same event would likely still escape by-eye detection in a lower-cadence field, while the $\Delta\chi^2_0$ would be lower by the same factor as the cadence. Four of the seven discovered planets had nominal cadences of $\Gamma = 4\,\mathrm{hr}^{-1}$, two (OGLE-2018-BLG-0516 and OGLE-2018-BLG-0977) had $\Gamma = 2\,\mathrm{hr}^{-1}$, and one (KMT-2019-BLG-0953) had $\Gamma = 8\,\mathrm{hr}^{-1}$.

[36] We say "diminished" rather than "prevented" because OGLE-2018-BLG-0677 (Herrera-Martin et al. 2020) was recognized by eye despite the fact that it was below the threshold of our machine search.

If we simply scale $\Delta\chi^2_0$ by Γ, then for KMTNet's seven $\Gamma = 1\,\mathrm{hr}^{-1}$ fields the seven $q < 2 \times 10^4$ discoveries listed in Table 12 would have $\Delta\chi^2_0 = (22, 56, 41, 98, 65, 35, 75)$. For these lower-cadence fields, the detection threshold will be set to $\Delta\chi^2_0 = 50$ (rather than 75) because the problem of contamination by low-level systematics is substantially reduced. Hence, four of the seven planetary events would have been investigated and plausibly published. On the other hand, for KMTNet's 11 $\Gamma = 0.4\,\mathrm{hr}^{-1}$ fields, the corresponding numbers are $\Delta\chi^2_0 = (9, 22, 16, 39, 26, 14, 30)$, which are clearly hopeless. The same applies, ipso facto, to KMTNet's three $\Gamma = 0.2\,\mathrm{hr}^{-1}$ fields.

Regarding higher mass-ratio planets, $q > 2 \times 10^{-4}$, these are generally much easier to identify by eye. Our preliminary review of the higher mass-ratio sample from the high-cadence fields confirms this assessment. The ratio of recovered-to-discovered planets that unambiguously have mass ratios $q < 2 < 10^{-4}$ is 4:7. For comparison there are 16 recovered planets with $2 \times 10^{-4} < q < 0.03$ in Table 11. If the recovered-to-discovered ratio were the same as for low-q planets, then we would expect 28 high-q discoveries. While we have not yet completed our investigation, we are confident that the actual number of high-q discoveries will be well below this number.

Thus, we expect that when our method is applied to lower-cadence fields it will generally recover the by-eye detected events, but the fraction of new discoveries will likely be smaller.

6.4. Conclusions

The KMTNet AnomalyFinder was applied to 2018–2019 prime-field data and returned 11 low mass-ratio ($q < 2 \times 10^{-4}$) planets, of which 4 were previously discovered by eye, 1 was previously reported in Paper I, and 6 are reported here for the first time. This 7:4 ratio suggests that many low mass-ratio planets are missed in by-eye searches. By contrast, there was only one by-eye discovery that was missed by AnomalyFinder, and this because it was below the χ^2 threshold of the algorithm.

While the investigation of the higher mass-ratio ($q > 2 \times 10^{-4}$) detections is not yet complete, a preliminary review suggests that by-eye searches are much more effective in this regime.

All six of the newly discovered low-q planets have higher angular offsets ($31^\circ < \alpha' < 74^\circ$) relative to the planet-host axis compared to the four previous discoveries ($6^\circ < \alpha' < 27^\circ$), which suggests that the "dilated" anomalies induced by acute trajectories are easier to discover by eye in the low-q regime (Jung et al. 2020b).

Combined, these results suggest that low mass-ratio planets may be more common than previously believed. However, systematic application of the AnomalyFinder to the lower-cadence fields and to additional seasons, combined with an efficiency analysis currently underway (Y. K. Jung et al., in preparation), will be required to make firm statements about this possibility.

Of the six planets reported in this paper, one could benefit from immediate AO observations. We found that the centroid of the blended light in KMT-2019-BLG-0253 lies within about 50 mas of the source and is most likely dominated by the lens or a companion to the lens. AO observations could greatly clarify or resolve the nature of this blend.

This research has made use of the KMTNet system operated by the Korea Astronomy and Space Science Institute (KASI), and the data were obtained at three host sites of CTIO in Chile, SAAO in South Africa, and SSO in Australia. Work by C.H. was supported by the grants of the National Research Foundation of Korea (2019R1A2C2085965 and 2020R1A4A2002885). The OGLE project has received funding from the National Science Centre, Poland, grant MAESTRO 2014/14/A/ST9/00121 to A.U. The MOA project is supported by JSPS KAKENHI grant Nos. JSPS24253004, JSPS26247023, JSPS23340064, JSPS15H00781, and JP16H06287. W.Z., S.M., X.Z., and H.Y. acknowledge support by the National Science Foundation of China (grant Nos. 11821303 and 11761131004). This research uses data obtained through the Telescope Access Program (TAP), which has been funded by the TAP member institutes. We are very grateful to the instrumentation and operations teams at CFHT that fixed several failures of MegaCam in the shortest time possible, allowing its return onto the telescope and these crucial observations.

ORCID iDs

Kyu-Ha Hwang https://orcid.org/0000-0002-9241-4117
Weicheng Zang https://orcid.org/0000-0001-6000-3463
Andrzej Udalski https://orcid.org/0000-0001-5207-5619
Hongjing Yang https://orcid.org/0000-0003-0626-8465
Shude Mao https://orcid.org/0000-0001-8317-2788
Michael D. Albrow https://orcid.org/0000-0003-3316-4012
Sun-Ju Chung https://orcid.org/0000-0001-6285-4528
Cheongho Han https://orcid.org/0000-0002-2641-9964
Youn Kil Jung https://orcid.org/0000-0002-0314-6000
Yoon-Hyun Ryu https://orcid.org/0000-0001-9823-2907
In-Gu Shin https://orcid.org/0000-0002-4355-9838
Yossi Shvartzvald https://orcid.org/0000-0003-1525-5041
Jennifer C. Yee https://orcid.org/0000-0001-9481-7123
Hyoun-Woo Kim https://orcid.org/0000-0001-8263-1006
Seung-Lee Kim https://orcid.org/0000-0003-0562-5643
Chung-Uk Lee https://orcid.org/0000-0003-0043-3925
Byeong-Gon Park https://orcid.org/0000-0002-6982-7722
Richard W. Pogge https://orcid.org/0000-0003-1435-3053
Przemek Mróz https://orcid.org/0000-0001-7016-1692
Jan Skowron https://orcid.org/0000-0002-2335-1730
Michał K. Szymański https://orcid.org/0000-0002-0548-8995
Igor Soszyński https://orcid.org/0000-0002-7777-0842
Paweł Pietrukowicz https://orcid.org/0000-0002-2339-5899
Szymon Kozłowski https://orcid.org/0000-0003-4084-880X
Krzysztof Ulaczyk https://orcid.org/0000-0001-6364-408X
Patryk Iwanek https://orcid.org/0000-0002-6212-7221
Marcin Wrona https://orcid.org/0000-0002-3051-274X
Mariusz Gromadzki https://orcid.org/0000-0002-1650-1518
Richard Barry https://orcid.org/0000-0003-4916-0892
David P. Bennett https://orcid.org/0000-0001-8043-8413
Akihiko Fukui https://orcid.org/0000-0002-4909-5763
Yuki Hirao https://orcid.org/0000-0003-4776-8618
Yoshitaka Itow https://orcid.org/0000-0002-8198-1968
Iona Kondo https://orcid.org/0000-0002-3401-1029
Naoki Koshimoto https://orcid.org/0000-0003-2302-9562
Shota Miyazaki https://orcid.org/0000-0001-9818-1513
Yasushi Muraki https://orcid.org/0000-0003-1978-2092
Greg Olmschenk https://orcid.org/0000-0001-8472-2219
Clément Ranc https://orcid.org/0000-0003-2388-4534
Nicholas J. Rattenbury https://orcid.org/0000-0001-5069-319X
Takahiro Sumi https://orcid.org/0000-0002-4035-5012
Daisuke Suzuki https://orcid.org/0000-0002-5843-9433
Matthew T. Penny https://orcid.org/0000-0001-7506-5640
Pascal Fouqué https://orcid.org/0000-0002-1436-7351

References

Alard, C., & Lupton, R. H. 1998, ApJ, 503, 325
Albrow, M. D. 2017, MichaelDAlbrow/pyDIA: Initial Release on Github, Zenodo, doi:10.5281/zenodo.268049
Albrow, M. D., Horne, K., Bramich, D. M., et al. 2009, MNRAS, 397, 2099
An, J. H., Albrow, M. D., Beaulieu, J.-P., et al. 2002, ApJ, 572, 521
Batista, V., Gould, A., Dieters, S., et al. 2011, A&A, 529, 102
Beaulieu, J.-P., Bennett, D. P., Fouqué, P., et al. 2006, Natur, 439, 437
Bennett, D. P., Bhattacharya, A., Beaulieu, J. P., et al. 2020, AJ, 159, 68
Bensby, T., Yee, J. C., Feltzing, S., et al. 2013, A&A, 549A, 147
Bessell, M. S., & Brett, J. M. 1988, PASP, 100, 1134
Bond, I. A., Abe, F., Dodd, R. J., et al. 2001, MNRAS, 327, 868
Bond, I. A., Bennett, D. P., Sumi, T., et al. 2017, MNRAS, 469, 2434
Bond, I. A., Udalski, A., Jaroszyński, M., et al. 2004, ApJL, 606, L155
Bozza, V. 2008, MNRAS, 408, 2188
Bozza, V., Bachelet, E., Bartolic, F., et al. 2018, MNRAS, 479, 5157
Calchi Novati, S., Suzuki, D., Udalski, A., et al. 2019, AJ, 157, 121
Chung, S.-J., & Lee, C.-U. 2011, MNRAS, 411, 151
Dong, S., Bond, I. A., Gould, A., et al. 2009, ApJ, 695, 970
Dong, S., Gould, A., Udalski, A., et al. 2009, ApJ, 695, 970
Duquennoy, A., & Mayor, M. 1991, A&A, 248, 485
Foreman-Mackey, D., Hogg, D. W., Lang, D., & Goodman, J. 2013, PASP, 125, 306
Gaudi, B. S. 2012, ARA&A, 50, 411
Gaudi, B. S., Albrow, M. D., An, J., et al. 2002, ApJ, 566, 463
Gaudi, B. S., & Gould, A. 1997, ApJ, 486, 85
Ghosh, H., DePoy, D. L., Gal-Yam, A., et al. 2004, ApJ, 615, 450
Gould, A. 1992, ApJ, 392, 442
Gould, A. 1996, ApJ, 470, 201
Gould, A. 2000, ApJ, 542, 785
Gould, A. 2004, ApJ, 606, 319
Gould, A. 2014, JKAS, 47, 215
Gould, A., Dong, S., Gaudi, B. S., et al. 2010, ApJ, 720, 1073
Gould, A., & Loeb, A. 1992, ApJ, 396, 104
Gould, A., Miralda-Escudé, J., & Bahcall, J. N. 1994, ApJL, 423, L105
Gould, A., Ryu, Y.-H., Calchi Novati, S., et al. 2020, JKAS, 53, 9
Gould, A., Udalski, A., An, D., et al. 2006, ApJL, 644, L37
Han, C. 2006, ApJ, 638, 1080
Han, C., Bennett, D. P., Udalski, A., et al. 2019, AJ, 158, 114
Han, C., Gould, A., Albrow, M. D., et al. 2021a, A&A, submitted
Han, C., Kim, D., Jung, Y. K., et al. 2020a, AJ, 160, 17
Han, C., Lee, C.-U., Udalski, A., et al. 2020b, AJ, 159, 48
Han, C., Shin, I.-G., Jung, Y. K., et al. 2020c, A&A, 641A, 105
Han, C., Udalski, A., Gould, A., et al. 2016, ApJ, 828, 53
Han, C., Udalski, A., Kim, D., et al. 2021b, A&A, 650, A89
Han, C., Udalski, A., Kim, D., et al. 2021c, AJ, 161, 270
Han, C., Udalski, A., Lee, C.-U., et al. 2021d, A&A, 649, A90
Herrera-Martin, A., Albrow, A., Udalski, A., et al. 2020, AJ, 159, 134
Holtzman, J. A., Watson, A. M., Baum, W. A., et al. 1998, AJ, 115, 1946
Jung, Y. K., Gould, A., Udalski, A., et al. 2019a, AJ, 158, 28
Jung, Y. K., Gould, A., Udalski, A., et al. 2020a, AJ, 160, 148
Jung, Y. K., Gould, A., Zang, W., et al. 2019b, AJ, 157, 72
Jung, Y. K., Han, C., Udalski, A., et al. 2021, AJ, 161, 293
Jung, Y. K., Udalski, A., Zang, W., et al. 2020b, AJ, 160, 255
Kervella, P., Thévenin, F., Di Folco, E., & Ségransan, D. 2004, A&A, 426, 297
Kim, D.-J., Hwang, K.-H., Shvartzvald, et al. 2018a, arXiv:1806.07545
Kim, D.-J., Kim, H.-W., Hwang, K.-H., et al. 2018b, AJ, 155, 76
Kim, S.-L., Lee, C.-U., Park, B.-G., et al. 2016, JKAS, 49, 37
Kim, Y. H. ., Chung, S.-J., Yee, J.-C., et al. 2021, AJ, 162, 17
Kondo, I., Yee, J. C., Bennett, D. P., et al. 2021, AJ, 162, 77
Nataf, D. M., Gould, A., Fouqué, P., et al. 2013, ApJ, 769, 88
Paczyński, B. 1986, ApJ, 304, 1
Park, B.-G., DePoy, D. L. ., Gaudi, B. S., et al. 2004, ApJ, 609, 166
Ranc, C., Bennett, D. P., Hirao, Y., et al. 2019, AJ, 157, 232
Ryu, Y.-H., Udalski, A., Yee, J. C., et al. 2020, AJ, 160, 183
Shvartzvald, Y., Yee, J. C., Calchi Novati, S., et al. 2017, ApJL, 840, L3
Skowron, J., Udalski, A., Gould, A, et al. 2011, ApJ, 738, 87
Smith, M., Mao, S., & Paczyński, B. 2003, MNRAS, 339, 925
Sumi, T., Bennett, D. P., Bond, I. A., et al. 2010, ApJ, 710, 1641
Suzuki, D., Bennett, D. P., Sumi, T., et al. 2016, ApJ, 833, 145
Szymański, M. K., Udalski, A., Soszyński, I., et al. 2011, AcAau, 61, 83
Tomaney, A. B., & Crotts, A. P. S. 1996, AJ, 112, 2872
Udalski, A. 2003, AcAau, 53, 291
Udalski, A., Ryu, Y.-H., Sajadian, S., et al. 2018, AcAau, 68, 1
Udalski, A., Szymanski, M., Kaluzny, J., et al. 1994, AcAau, 44, 227
Wang, H., Zang, W., Zhu, W., et al. 2021, in press
Woźniak, P. R. 2000, AcAau, 50, 421
Yee, J. C., Zang, W., Udalski, A., et al. 2021, AJ, 162, 180
Yoo, J., DePoy, D. L., Gal-Yam, A., et al. 2004, ApJ, 603, 139
Zang, W., Han, C., Kondo, I., et al. 2021a, RAA, 21, 239
Zang, W., Hwang, K.-H., Udalski, A., et al. 2021b, AJ, 162, 163
Zang, W., Penny, M. T., Zhu, W., et al. 2018, PASP, 130, 104401